Thesis for the degree of Doctor of Philosophy

Effects of Irradiation and Thermal Ageing on the Nanoscale Chemistry of Steel Welds

Kristina Lindgren

Department of Physics

Chalmers University of Technology

Göteborg, Sweden 2018

Effects of Irradiation and Thermal Ageing on the Nanoscale Chemistry of Steel Welds
Kristina Lindgren

ISBN 978-91-7597-825-3

Doktorsavhandlingar vid Chalmers tekniska högskola
Ny serie nr 4506
ISSN 0346-718X

Department of Physics
Chalmers University of Technology
SE-412 96 Göteborg
Sweden
Telephone + 46 (0)31-772 1000

Cover illustration
Left: an atom probe tomography reconstruction of the irradiated Ringhals R4 reactor pressure vessel surveillance material. The enlarged volume is $10 \times 10 \times 10\,\mathrm{nm}^3$. Middle: thermally aged Ringhals R4 pressurizer weld metal. Right: irradiated Zorita core barrel weld, a loop is shown in the box. All isoconcentration surface thresholds and identities are given in the figure.

Printed by Chalmers Reproservice
Göteborg, Sweden 2018

Effects of Irradiation and Thermal Ageing on the Nanoscale Chemistry of Steel Welds
Kristina Lindgren
Department of Physics
Chalmers University of Technology

Abstract

Structural materials of nuclear power plants degrade during operation due to thermal ageing and irradiation from the reactor core. Effects on the materials are an increase in hardness and tensile strength, and a decrease in ductility and fracture toughness, i. e. embrittlement. The degradation of the mechanical properties stems from changes in the microstructure. In this thesis, the effects of thermal ageing and irradiation on the nanoscale chemistry has been studied using atom probe tomography (APT).

During irradiation, nanometre sized clusters are formed in the reactor pressure vessel (RPV) welds. As the RPV is a life-limiting part of a nuclear power plant, neutron irradiation with high flux is attractive for accelerated studies. Here, the effect of high flux is found to result in a higher number density of smaller NiMnSi-rich clusters for the high Ni and Mn - low Cu welds from Ringhals R4, resulting in similar hardening compared to surveillance material. It is also found that there are some *stable matrix defects* formed in the high flux material, contributing to the embrittlement. The cluster evolution showed no signs of *late blooming phases* (an accelerated degradation at high fluences). Furthermore, thermal ageing during operation for 28 years of a weld from the former Ringhals R4 pressurizer with similar composition is found to result in clusters forming mainly on dislocations, hardening the weld metal.

In ferrite with higher Cr-content, such as the ferritic parts of the mainly austenitic welds from the core barrel of the decommissioned Spanish reactor José Cabrera, spinodal decomposition occurs as well as G-phase ($Ni_{16}Si_7Mn_6$) precipitation. Weld metals irradiated up to 2 dpa are compared with thermally aged welds, confirming that the irradiation is considerably contributing to the changes in the microstructure. After 0.15 dpa, the spinodal decomposition was well developed, and the Cr concentration in the ferrite was found to influence the wavelength more than the difference in irradiation (0.15 to 2 dpa). The G-phase precipitates were more well-developed after 1 dpa neutron irradiation, but no difference could be distinguished between the material irradiated to 1 and 2 dpa.

Keywords: reactor pressure vessel, irradiation damage, thermal ageing, clustering, atom probe tomography, low alloy steel, core barrel, spinodal decomposition

Preface

The research work presented in this thesis was carried out at the Division of Materials Microstructure at the Department of Physics, Chalmers University of Technology, during the time period June 2014 - December 2018, under the supervision of Associate Professor Mattias Thuvander and Professor Krystyna Stiller.

List of appended papers

I. *On the analysis of clustering in an irradiated low alloy reactor pressure vessel steel weld*
K. Lindgren, K. Stiller, P. Efsing, and M. Thuvander
Microscopy and Microanalysis 23, 376-384 (2017)

II. *Evolution of precipitation in reactor pressure vessel steel welds under neutron irradiation*
K. Lindgren, M. Boåsen, K. Stiller, P. Efsing, and M. Thuvander
Journal of Nuclear Materials 488, 222-230 (2017)

III. *Cluster formation in in-service thermally aged pressurizer welds*
K. Lindgren, M. Boåsen, K. Stiller, P. Efsing, and M. Thuvander
Journal of Nuclear Materials 504, 23-28 (2018)

IV. *Thermal ageing of low alloy steel weldments from a Swedish nuclear power plant - the evolution of the microstructure*
K. Lindgren, M. Boåsen, K. Stiller, P. Efsing, and M. Thuvander
Proceedings of Fontevraud 9: Contribution of Materials Investigations and Operating Experience to Light Water NPPs Safety, Performance and Reliability (2018)

V. *Post irradiation annealing of high flux irradiated reactor pressure vessel weld*
K. Lindgren, M. Boåsen, P. Efsing, K. Stiller, and M. Thuvander
In manuscript

VI. *Integrated effect of thermal ageing and low flux irradiation on microstructural evolution of welded stainless steels*
K. Lindgren, M. Bjurman, P. Ekström, P. Efsing, and M. Thuvander
In manuscript

Publications not included in this thesis

Development of matrix microstructure in polycrystalline cubic boron nitride ceramics
K. Lindgren, A. Kauppi and L. K. L. Falk
Journal of the European Ceramic Society 37, 3017-3026 (2017)

Interplay of water and reactive elements in oxidation of alumina-forming alloys
N. Mortazavi, C. Geers, M. Esmaily, V. Babic, M. Sattari, K. Lindgren, P. Malmberg, B. Jönsson, M. Halvarsson, J. E. Svensson, I. Panas and L. G. Johansson
Nature Materials 17, 610-617 (2018)

Microstructural Evolution of Welded Stainless Steels on Integrated Effect of Thermal Aging and Low Flux Irradiation
M. Bjurman, K. Lindgren, M. Thuvander, P. Ekström and P. Efsing
Proceedings of the 18th International Conference on Environmental Degradation of Materials in Nuclear Power Systems -Water Reactors, 703-710 (2018)

Thermal ageing of low alloy steel weldments from a Swedish nuclear power plant - a study of mechanical properties
M. Boåsen, K. Lindgren, J. Roudén, M. Öberg, J. Faleskog, M. Thuvander and P. Efsing
Proceedings of Fontevraud 9: Contribution of Materials Investigations and Operating Experience to Light Water NPPs Safety, Performance and Reliability (2018)

Thermal aging of cast and welded stainless steels on LTO and the influence of the change of reactor materials
M. Bjurman, M. Thuvander, K. Lindgren, and P. Efsing
Proceedings of Fontevraud 9: Contribution of Materials Investigations and Operating Experience to Light Water NPPs Safety, Performance and Reliability (2018)

My contributions to the appended papers

I. Performed the APT measurements, specimen preparation by FIB/SEM lift-out, data analysis and interpretations, and wrote the paper with input from the co-authors.

II. Performed the APT measurements, data analysis and interpretations, specimen preparation by FIB/SEM lift-out, and wrote the paper, with input from co-authors. The hardness measurements were not performed by the first author.

III. Performed the APT measurements, data analysis and interpretations, specimen preparation by electropolishing, and wrote the paper, with input from co-authors. The hardness measurements were not performed by the first author.

IV. Performed the APT measurements, data analysis and interpretations, specimen preparation by FIB/SEM lift-out and electropolishing, and wrote the paper, with input from co-authors.

V. Performed the APT measurements, data analysis and interpretations, specimen preparation by FIB/SEM lift-out, and wrote the paper, with input from co-authors.

VI. Performed the APT measurements, data analysis and interpretations, specimen preparation by FIB/SEM lift-out, and wrote the paper, with input from co-authors.

Contents

CHAPTER 1

Introduction

There is a worldwide increasing demand of energy as the population increases. Access to electric energy is of great importance, it can be considered as one of the backbones of modern society, for the industry as well as for the individual. At the same time, the world is facing the challenge of climate change due to the emission of CO_2. In this perspective, the nuclear power plays a role in a mix of many different sources of electricity with low or no CO_2 emission such as hydro, solar, wind as a stable and reliable source of electricity. In the 2018 report from the Intergovernmental Panel on Climate Change (IPCC) on the global warming, electricity from nuclear power is part of their four possible future scenarios on how the global warming could be limited to 1.5 °C [1]. Today, around 11% of the global electricity is produced by nuclear power [2]. In Sweden, the corresponding number is 40% [2, 3].

Needless to say, the energy has to be produced in a safe way. Today, many nuclear power plants in operation are approaching their estimated end of life. In some cases, the lifetime of the reactors is extended (with constant checks of the performance of the reactor). Thus, it is important to understand how long-time operation is affecting the power plant in order to make accurate estimates of the degradation. In Sweden, the nuclear reactors in use were commissioned between 1972 and 1985, with an original designed life-time of 40 years, and thus understanding the effects of ageing is of importance [4]. Extension of

operation of Swedish power plants is based on regular assessments of safety [5].

The environment in the nuclear reactor poses requirements on the structural materials used. The neutron irradiation will affect the materials, leading to a degradation of the mechanical properties. Internal structures will thus degrade with time as a result of the conditions during the operation of the power plant.

The neutron fluence affecting the reactor pressure vessel (RPV) is much lower than for the internal parts. However, the RPV is very complex to replace, so complex that it is not done in practice. During the operational times of years the neutrons interact with the low alloy steel and degrade the mechanical properties. The reactor pressure vessel metal is embrittled due to cluster[1] formation in the material, at the nanometre scale. The nanometre sized clusters hinder dislocation glide and thus contribute to the embrittlement of the material. Therefore, it is important to understand the cluster formation and evolution, and the connection to the mechanical properties.

1.1 Aim of this study

This research was undertaken in order to characterise the development of the microstructure in the low alloy RPV steel weld identical to welds in Ringhals R4, and the thermally aged pressurizer from the same reactor. The Ringhals RPV welds are known for having a high Ni and Mn content, and low Cu content, giving an unexpectedly large change in mechanical properties after irradiation [6]. Atom probe tomography (APT) has been used in order to study the nanometre size clusters formed during irradiation and thermal ageing. There are not many techniques available to characterise nanometre clusters; APT offers high resolution information (position and identification of atoms) in both depth and lateral directions. Thus, it is well suited for characterising the clusters of interest. This project is part of the Måbil (Material, Åldring, Bränsle inom Lärosätesverksamheten) project that is funded by the Swedish Centre of Nuclear Technology (SKC). Funding was also provided by the Nordic Nuclear Safety Research (NKS) collaboration.

In addition to the RPV weld metal, welds from the core barrel, from the decommissioned reactor José Cabrera (Zorita), Spain, is studied using the same technique. In the ferrite part of these materials, spinodal decomposition and formation of nanometre sized G-phase precipitates are the effects of the neutron irradiation, leading to embrittlement of the material. This part of the

[1] The terms precipitates and agglomerates are also commonly used. In this thesis the word cluster is used most of the time, although they in some cases might be precipitates with separate crystallographic structure from the matrix. In *Paper II* the term precipitates is used. Using only APT, the distinction cannot be made.

project is funded by the Electric Power Research Institute (EPRI) and the Swedish Radiation Safety Authority (SSM).

The objectives of this study are:

- To study the evolution of nanometre sized clusters containing Ni, Mn, Si and Cu that are formed during irradiation of the low Cu, high Ni and Mn welds of Ringhals R4 RPV, and to understand their connection to the mechanical properties. There is a theory on so called *late blooming phases* appearing in high Ni, low Cu materials, that would lead to a fast degradation of the mechanical properties after considerable time of operation [7]. These are also looked for in the materials as this would affect the possibilities of extended lifetime of the entire reactor. Furthermore, the influence of flux on the clustering is studied, in order to explain the apparent non-existing difference in mechanical properties of the R4 welds after irradiation inside the reactor (surveillance material) and weld metal irradiated in a higher flux in a materials test reactor (MTR) [8]. This is an important step if the higher flux material is to be used for mechanical testing to describe and predict the degradation of the reactor in operation.

- To study the effects of thermal ageing in the R4 pressurizer welds, that have been in operation for around 28 years at 345 °C. The welding specifications of the R4 pressurizer are the same as these of the Ringhals R4 RPV. The long ageing time is unusual, as many studies are made on materials thermally aged at higher temperatures for shorter times in order to accelerate the ageing, for practical reasons. It is thus a unique opportunity to study long-term thermal ageing at the actual operating temperature. The mechanical properties of the pressurizer are less affected by the ageing than the RPV, but still the change was larger than anticipated from the construction of the power plant. It turned out that the pressurizer contained nanometre sized clusters after ageing, and since they are formed purely by thermal effects they are well suited for comparison with the clusters in the irradiated material.

- To characterise the effects of neutron irradiation and thermal ageing of the remaining ferrite in austenitic welds from internal parts of the José Cabrera reactor and Ringhals R2. This is an opportunity to study spinodal decomposition and G-phase formation in material subjected to realistic operating conditions.

CHAPTER 2

Background

In this chapter, some of the background to the thesis is given. First, the components of a nuclear reactor and their functions are described, then the effects of neutron irradiation and thermal ageing on low alloy steels are discussed. The chapter is concluded with a description of spinodal decomposition and G-phase formation in the ferrite phase of internal, stainless steel, components.

2.1 The Nuclear Reactor

The RPV is an important structural part of the nuclear power plant. It acts as a container of the central parts of the reactor. The core with the UO_2 fuel is placed inside the RPV; the fission process takes place here. ^{235}U is fissile and is used as fuel in most nuclear power plants in operation. The fission takes place through a series of chain reactions. As the natural abundance of ^{235}U is low (0.7%, the most abundant isotope being ^{238}U) the fuel is enriched to 3 to 5% before the manufacturing of the fuel. In the nuclear power plant, the heat from the fission process is converted into electricity. In light water reactors (LWRs) water is used as both coolant and moderator of the neutrons created in the fission process. The neutrons are attenuated by the water (mainly by the hydrogen atoms) in the reactor, since the cross section of the fission reactions

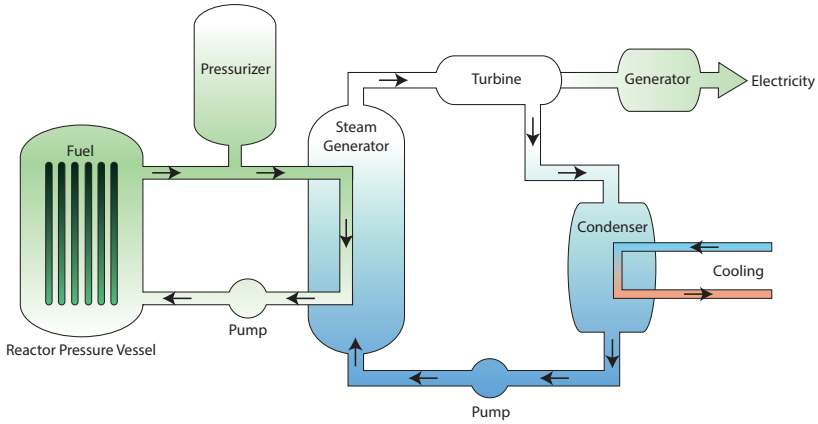

Figure 2.1: Schematic of a pressurised water reactor.

is higher for neutrons with low energy (thermal neutrons).

There are two main types of LWRs, boiling water reactors (BWRs) and pressurised water reactors (PWRs). A BWR consists of one circuit where water is heated and steam is driving the generator. A PWR has two systems; one primary circuit, where the pressure is kept by the use of a pressurizer in order to prevent the water from boiling [9], see Figure 2.1. The pressure of the system is increased by turning on heaters in the pressurizer, and decreased by spraying cool water in the pressurizer. In the secondary circuit, steam is generated and used in the turbine to produce electricity. Due to the differences in design, BWRs and PWRs have different operational temperatures and pressures; a PWR 280-325 °C and about 15 MPa, and a BWR 280-288 °C and about 7 MPa [10]. The RPVs are exposed to different neutron fluences during the life time of the reactor; a PWR has a higher exposure due to a smaller RPV diameter and hence less water between the RPV and the fuel. The materials analysed in this thesis all originate from PWRs.

2.1.1 Reactor Pressure Vessel Construction

The RPV is a life-limiting part of a reactor; it is very complex to replace, and replacement is thus not done in practice. The RPV is constructed from a low alloy steel, and clad with stainless steel on the inside for corrosion resistance. The demands on the RPV are high; high strength and fracture toughness, low ductile-to-brittle transition temperature (DBTT), homogeneous mechanical properties, and good weldability are of importance [9]. The low alloy steel is chosen due to its resistance to thermal stresses [11]. Some alloying elements

are added, for instance Ni for increased fracture toughness and forgeability, Mn for binding sulfur (that otherwise acts embrittling), and Si as a deoxidiser [12]. P and Cu are impurity elements that are known to affect the irradiation susceptibility [13, 14].

The RPVs of the PWRs R3 and R4 in Ringhals are 13 m high, have an inner diameter of 4 m, consist of 20 cm thick steel and weigh 330 tonnes [15]. There are different ways of producing RPVs. One way is to weld forged rings together, using only circumferential welds. Another way to produce the RPV is to start with plates that are bent, and join them with both longitudinal and circumferential welds. It is beneficial to avoid longitudinal welds, in particular in the core (belt-line) region, due to the stress distribution in the vessel.

In order to follow the degradation of the RPV, surveillance specimens are put inside the reactor. In this way, the specimens are irradiated faster (and with a higher flux) than the RPV steel itself, making it possible to remove the surveillance specimens and perform mechanical testing and characterisation of the material.

The construction of the pressurizer is in many ways similar to the RPV. The material is the same, and hence the welds are similar to the RPV welds. The pressurizer is in general smaller than the RPV. Ringhals R4 pressurizer, is for instance 12.8 m high, has an inner diameter of 2.4 m and a weight of 82 tonnes [16]. The pressurizer is not exposed to neutron irradiation, and the temperature inside is slightly higher than in the RPV. It is possible to replace the pressurizer, as was done for Ringhals R4 during the revision in 2011 [16].

2.1.2 The Welds of the Reactor Pressure Vessel

Welding is used to join pieces together, in order to create a joint with no leakage; molten metal is used to fill the gap of the pieces to be joined. The welding affects the microstructure of the RPV material; some different zones can be considered. The base material some distance from the weld is not affected by the welding. The volume close to the weld is known as the heat affected zone. The structure of the weld itself is different from the base metal and might have a different chemical composition dependent on the selection of filler metal. The welding parameters such as voltage, current, and speed, as well as the cooling rate have an impact on the microstructure. Fast cooling results in martensite (having unwanted mechanical properties - it is too hard and brittle). The cooling rate depends on the heat input, and thickness and temperature of the plates. Solidification occurs in a dendritic fashion, giving segregation and compositional variations within the weld [12].

Figure 2.2: Cross-section of a pressurizer weld from Ringhals. The inside (top part in photo) is clad with stainless steel to enhance corrosion resistance.

Welds usually have a higher alloying element content than the base material. This could make the welds more sensitive to radiation and heat and thus, in many reactors, they can be said to be the part of the RPV that is most susceptible to irradiation induced embrittlement.

There are different welding methods, used for different situations. The type of welding used in the RPV is called submerged arc welding (SAW). SAW has high productivity and is always automated, and it is used to join thick plates. For SAW an electrode (filler metal) is used. The filler metal might have a different chemical composition than the base material in order to achieve specific properties. In RPV steel welds the Cu content origins from the filler metal and the coating on the filler metal [14] that increases the electrical conductivity and decreases the wear on the equipment. Both the filler and plates are melted under a layer of flux powder, thus the term submerged. In this way, sparks are avoided. In Figure 2.2 an SAW weld can be seen. The plates have noses into the weld that are needed as a result of the geometrical limitations due to the thickness of the material. After welding, the weld is subjected to a post weld heat treatment (PWHT) in order to achieve the desired mechanical properties and to release stresses. A typical PWHT temperature is around 600 °C.

2.1.3 Internal Components

Inside the RPV, there are many internal structures, such as tubes, structures holding the fuel and control rods in place, and shielding the vessel from the neutrons. One of these internal structures is the core barrel. The water of the primary circuit enters the RPV from the side, then it flows down between the RPV wall and the core barrel. It then flows through the core barrel where the fuel rod assemblies are located, and gets heated. Many of the internal components are made out of austenitic stainless steel (with some remaining ferrite in the welds).

2.2 Irradiation Damage of the Reactor Pressure Vessel

The RPV is affected by the neutrons emitted from the fission process. The irradiation damage time scale spans over many orders of magnitude; neutrons interact with atoms in the bulk material and cascades are created on the picosecond scale (10^{-12} s), whereas the lifetime of a reactor is in the order of 40-60 years (10^{9} s). Due to the short time scale and the small length scale of the initial damage, experimental data on the damage process cannot achieved in-situ. The damage can be studied by modelling on different scales, and the effect on mechanical properties and microstructure can be characterised experimentally using various techniques.

The neutron flux is low, in fact the RPV is subjected to low fluences in a life-time; in around 40 years it is subjected to 0.0075 - 0.24 displacements per atom (dpa) corresponding to $5 \cdot 10^{22}$ n/m^2 to $1.6 \cdot 10^{24}$ n/m^2, compared to internal elements such as fuel cladding tubes and internal spacer grids that get doses up to 80 dpa or $5 \cdot 10^{26}$ n/m^2 [10]. However, the interaction with the neutrons is enough to affect the mechanical properties of the RPV weld metal. It is mainly the belt-line region that is subjected to neutron damage due to the geometry of the reactor i. e. due to the vicinity to the fuel. Other parts, such as the RPV head, are not affected by the neutron radiation.

In order to understand the evolution of the mechanical properties, the structural changes of the irradiated material can be studied. The connection between the mechanical properties and the microstructure is a link to further be able to understand the mechanisms and predict the ageing process.

A standard method to characterise the embrittlement of irradiated RPV welds is impact testing, or Charpy V-notch testing [7]. In short, the energy absorbed during fracture is measured. The specimen is in the shape of a bar with a pre-prepared notch. The measurement is repeated several times at different temperatures to obtain a curve of absorbed energy as a function of temperature.

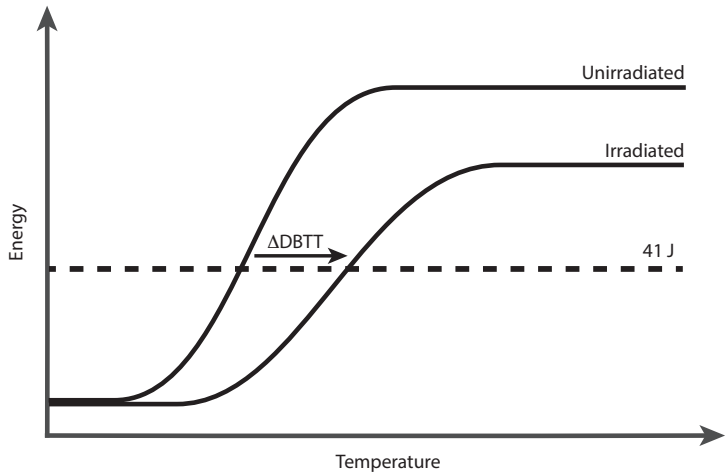

Figure 2.3: Schematic ductile-to-brittle transformation temperature shift for RPV steels measured by Charpy impact testing. The DBTT is often given at 41 J.

At some temperature the behaviour of a bcc material will change from brittle (low temperatures, low energies absorbed) to ductile (high temperatures, more energy absorbed). This can be illustrated by the ductile-to-brittle-transition temperature (DBTT), commonly given at 41 J, see Figure 2.3. The irradiation leads to an increase in the DBTT and in a reduction of the upper shelf energy, reducing the energy absorbed at fracture by the Charpy specimen for high temperatures.

Both tensile testing and hardness measurements can also be performed in order to characterise the ageing of the steel. For Vickers hardness test a pyramid-shaped indent is pushed with a known force into the material, and the resulting area of the indentation is measured. Thus, the amount of material needed is smaller than for Charpy V testing. However, not all the embrittling processes are hardening - for instance the segregation of P to grain boundaries is not, but it affects the possibility of intergranular cracking and can lead to embrittlement without affecting the hardness [17–19].

2.2.1 Direct Matrix Damage

Neutrons with an energy spectrum from 0.025 eV (thermal neutrons) up to 17 MeV are produced in the reactor [20]. The lowest neutron energy needed to damage the RPV material is considered to be between 0.5 and 1 MeV (fast neutrons), dependent on reactor design. For western reactors, 1 MeV is used as the threshold energy for the neutrons to be included in the given fluence.

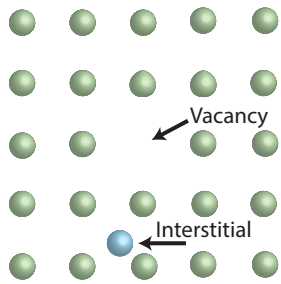

Figure 2.4: Schematic of a Frenkel pair. After a few picoseconds many of the Frenkel pairs have been annihilated by recombination.

The neutron interacts with an Fe lattice atom with a relatively low probability and might therefore travel some distance (in the order of centimeters) in the bulk of the material. The first atom the neutron collides with is known as the primary knock-on atom (PKA). The PKA will receive energy from the neutron and leaves it position, creating a cascade, knocking out other atoms in its path in volumes with sizes of a few nanometers. The neutron of the collision will continue to hit matrix atoms that create new cascades until the neutron energy is too low. For bcc Fe, the displacement threshold energy is around 40 eV [10].

A Frenkel pair, consisting of one vacancy and one interstitial is illustrated in Figure 2.4. Most of the Frenkel pairs created during neutron irradiation are recombined within a few picoseconds. The vacancies and interstitials that do not recombine might interact with other features in the vicinity and affect the microstructure by increasing the diffusion, which without irradiation is so low that almost no significant diffusion takes place at reactor temperatures during the lifetime of the RPV.

Matrix defects, such as interstitial loops and small clusters of vacancies, too small to study using transmission electron microscopy (TEM), are affecting the RPV yield strength [21–25]. The contribution of matrix defects, which are stable at reactor temperatures, to the yield strength is commonly considered to be proportional to the square root of neutron fluence ($\Delta\sigma_{y,matrixdefects} \propto \sqrt{\phi t}$) [26, 27], where ϕ is the flux, t is the time, and thus ϕt the fluence). In general, the contribution from matrix defects to the embrittlement is considered to be small in comparison to the effect of alloy element clusters [28].

There are also matrix defects that are unstable at operational temperatures, i. e. they might reach a steady state number density, where they are created and annihilated at the same rate. The presence of matrix defects is affected by the material composition and the irradiation, for instance the neutron flux [29]. For low fluxes (such as normal operation in a reactor or in surveillance mate-

rial) no unstable matrix damage remains in some materials [30, 31] whereas increased flux (above around 10^{16} n/(m^{2}s), such as in MTRs) gives an unstable matrix damage contribution under some conditions [32].

2.2.2 Solute Clustering

In general, two different families of nanometre sized clusters[1] are considered to form during irradiation in RPV welds; Cu-rich clusters and NiMnSi-rich clusters, dependent on the composition of the weld [33–38]. There is no strict boundary between them composition-wise; Cu-rich clusters contain some Ni, Mn and Si, but smaller amounts than the NiMnSi-rich clusters, that in turn most often also contain some Cu. Their difference in composition suggests differences in formation mechanisms. The composition of the clusters is dependent on the composition of the weld, low-Cu welds ($< 0.1\%$) give NiMnSi-rich clusters, such as in the irradiated Ringhals RPV material analysed in this project. The clusters can be found on dislocation lines as well as in the matrix [39–41].

A relatively high Cu content (up to 0.4%) was found to be detrimental for mechanical properties after neutron irradiation in the late 1960s. The high Cu was found to correlate with more embrittlement, that in turn was found to be due to the formation of Cu-rich clusters forming during irradiation [42–45]. After this insight, many RPV steel welds were fabricated containing less Cu. The small, Cu-rich clusters formed during irradiation are believed to be too small for being separate phases (thermally aged RPV steels might however contain larger precipitates with other crystal structures such as 9R [46]). The Cu-rich clusters are believed to form due to supersaturation of Cu in bcc Fe; the solubility of Cu is very low, around 30-42 atomic parts per million (appm) at RPV relevant temperatures [7, 47]. Strong Ni-Mn bonds and the interfacial energy towards the Fe in the matrix often result in a Cu-rich core with a shell of Ni and Mn atoms [32, 48, 49]. The cluster formation results in hardening. The effect of Cu precipitation on DBTT is generally considered to be saturating, due to the depletion of Cu from the matrix.

Odette et al. stated that the effect on mechanical properties of NiMnSi-rich clusters can be accelerated at high fluence and gave them the name *late blooming phases* [7, 32, 34]. The phenomenon and its naming is a matter of discussion, with some results pointing towards them not being late blooming, or precipitates [50]. In this thesis, the term NiMnSi-rich clusters is used, with no assumptions made on their crystal structure and whether they bloom late or not.

[1] See earlier footnote on cluster/precipitate/agglomeration choice of vocabulary.

The formation of NiMnSi-rich clusters is a matter of more discussion than the formation of the Cu-rich clusters. The Ni, Mn and Si contents are all below the solubility limit in Fe-Ni, Fe-Mn and Fe-Si binary alloys [23], and thus supersaturation should not be the driving force, unless the synergy between the alloying elements drastically changes the solubility limits. The NiMnSi-rich clusters generally form in RPV weld metals with low Cu and high Ni content. The formation is believed to be accelerated by Cu, in terms of clustering on Cu embryos [51, 52]. However, examples are found where NiMnSi-rich clusters form in Cu-free steels [47], and in low-Cu steels, but without any Cu atoms in the clusters [53].

The thermodynamic stability of the clusters is a matter of debate, with some claiming that they are not stable [50, 54, 55], i. e. they would not grow in the absence of the point defects created by neutron irradiation. Monte Carlo simulations show that the role of self-interstitials and vacancies in the formation is vital and that the growth of clusters without Cu is slower than the growth of Cu-rich clusters [50, 56]. The NiMnSi-rich clusters are believed to form on small interstitial loops, which are immobilised by solute atoms, primarily Mn and Ni [57]. In Fe-Mn model alloys, Mn has been observed to significantly increase the number of loops during neutron irradiation [58]. The loops are generally not observable by TEM, in a RPV steel they would be below the size when they can be detected [10]. Other solute atoms (Ni, Mn, Si, Cu, and P) are dragged there by vacancies and by a dumbbell mechanism occurring in irradiated materials (only Mn and P) [56, 59]. Kinetic object Monte Carlo simulations using this model give an estimated number of interstitial loops that corresponds well to the number density of NiMnSi-rich clusters in the irradiated Ringhals surveillance material as detected by APT [59]. Other results are pointing towards thermodynamically stable precipitates due to synergetic effects between Ni, Mn and Si, describing the NiMnSi-rich clusters as intermetallic phases, such as Γ_2 or G-phase, based on thermodynamic models [60], X-ray diffraction [61], and comparing compositions to APT results [51, 62]. The transition from a relatively matrix coherent cluster to for instance G-phase is then vital, with results pointing towards a lower energy after such transition, but density functional theory simulations show that it is uncertain whether all requirements for such a transition are met [63].

The beginning-of-life mechanical properties of the high-Ni RPV steel welds are good, but the impact of irradiation during operation needs to be further understood [64, 65]. This is one of the motivations of this thesis.

The neutron flux, i. e. the number of neutrons per time and unit area, is known to affect the cluster characteristics [66, 67]. As the entire reactor would have to permanently be closed down in order to obtain material from the RPV, surveillance material irradiated inside the reactor at higher flux is commonly analysed. A typical flux in such materials is usually around four times higher

than in the RPV (a lead factor equal to four) [5, 68]. Furthermore, materials irradiated in MTRs for a few weeks or months instead of years are also of interest, having an even higher neutron flux. The clustering of solute elements is affected by the higher flux due to an increase in diffusion as the number of Frenkel pairs at any given time is higher. The result of a higher flux is commonly smaller clusters with higher number density [66, 69–72]. In this thesis, the effects of flux on high Ni and Mn content Ringhals R4 welds are investigated.

2.2.3 Segregation to Grain Boundaries

The matrix defects created by the fast neutrons lead to increased diffusion in the material. Point defects (vacancies and interstitials) will move towards grain boundaries that act as sinks, resulting in radiation induced segregation (RIS). The effect can be explained as the inverse Kirkendall effect [9, 26]. When considering the flow of vacancies towards the grain boundary, this must be followed by an equal flow of atoms in the opposite direction. If the net flow of one type of atoms is smaller than for an other type of atoms, this results in the first type of atoms having higher concentrations at the grain boundary. In the same way, the net flow of interstitials may also vary for different atomic spieces. In RPV weld metals, P tends to segregate to grain boundaries when the material is irradiated [73, 74], increasing the risk of intergranular failure and thus having an embrittling effect. A higher P content, but also higher temperature, fluence, and Ni content in the material result in more segregation to grain boundaries [13, 73]. C segregated to grain boundaries will, on the other hand, have a positive effect by strengthening the boundary [75, 76]. In this thesis, the effects of segregation to grain boundaries are not further looked into.

2.2.4 Impact of Features on Mechanical Properties

The ductility of the RPV is connected to the ability of line dislocations to move within the material. As long as the dislocations can move freely, the material can be deformed without fracture and is thus ductile. However, during irradiation, the clusters and the matrix damage form obstacles for the dislocations in the RPV, and the material becomes less ductile. One way of describing the bowing of dislocations around obstacles, hindering the dislocation glide, is the dispersed barrier hardening (DBH) model, contributing to the yield strength as

$$\Delta\sigma_y = \alpha M G b \sqrt{N d} \tag{2.1}$$

where M is the Taylor factor (close to 3), G is the shear modulus, b is the Burgers vector, N is the number density and d is the mean diameter of the feature. α is the strength of the barrier; $\alpha = 1$ is the case of Orowan hardening, meaning that line dislocations bow around the barrier [26, 69, 77].

The clusters contribute to the yield strength in terms of dispersed barrier hardening (equation 2.1). The values of α are reported to be $0.10 - 0.15$ [36, 69, 78]. The clusters have high number density, and thus they contribute to a large part of the increased strength i. e. the embrittlement of the material.

Another model that is commonly used for the cluster contribution to the yield strength is the Russell-Brown (RB) model [79]. This model describes the cluster contribution as

$$\Delta\sigma_y = \frac{MGb}{L}\Big(1 - \frac{E_1^2}{E_2^2}\Big)^{3/4} \tag{2.2}$$

with

$$L = \frac{\sqrt{\pi}d}{2\sqrt{f_v}} \tag{2.3}$$

and

$$\frac{E_1^2}{E_2^2} = \frac{E_1^\infty \log\frac{d}{2r_0}}{E_2^\infty \log\frac{R}{r_0}} + \frac{\log\frac{2R}{d}}{\log\frac{R}{r_0}} \tag{2.4}$$

where L is the spacing between clusters in the slip plane, f_v is the cluster volume fraction, $\frac{E_1^\infty}{E_2^\infty}$ is the ratio of the energies per unit length of dislocation in infinite media, and R and r_0 are the outer and inner cut off of the dislocations, respectively.

In addition to the models above, it is common to show a correlation between the square root of the volume fraction of the precipitates and the hardness (see for instance [80–82]). Assuming small variations in cluster size, both models above have a square root dependence of the volume fraction on strength.

2.3 Thermal Ageing of Reactor Pressure Vessel Steels

Thermal ageing can also contribute to embrittlement of RPV steels. In an LWR, the temperature in the RPV (around 290 °C) is generally considered to be too low for thermal ageing to occur due to the slow diffusion of solute elements [83]. However, there are other parts in the primary loop that have higher temperatures such as the pressurizer of a PWR. Furthermore, thermally aged materials are studied to compare with, and as a complement to, irradiated materials. The composition of the welds affects the temperature needed for thermal ageing to happen, for instance a combination of high Ni (1.66 at.%)

and high Cu (0.44 at.%) gives a significant hardness increase (80 HV) after 100,000 h at a temperature as low as 330 °C [84], whereas 140,000 h at 310 – 320 °C had no impact on hardness in VVER-1000 weld metals with similar Ni content but considerably lower Cu contents (0.03-0.09 wt.%) [18].

The effect of thermal ageing is similar to that of radiation damage, solute clustering[2] of Cu, Ni, Mn and Si, and possibly segregation of P to grain boundaries due to increased diffusion, take place [17, 18, 84, 85]. However, there is no matrix damage, as there are no neutrons interacting with the atoms, creating cascades. The increase in diffusion with temperature is thus due to only vacancies dragging the solutes, as there are no self-interstitials in the absence of irradiation. The cluster formation is driven by the low Cu solubility in Fe. Just as in the irradiated material, Ni, Mn, and Si are known to reduce the interfacial energy between the Cu and the Fe, and thus form a shell around the Cu-rich core, as seen in simulations [86, 87], and as observed using APT [84, 88–90] in model alloys and RPV materials. In high Cu RPV materials (0.32-0.55 at.%), Hyde et al. found that thermal ageing results in clusters with a higher Cu content than the clusters in the same material when irradiated [88]. In this thesis, the pressurizer welds of Ringhals R4 (with high Ni and Mn, and low Cu content) that have been in operation, i. e. thermally aged, for 28 years (190,000 h) at 345 °C are analysed.

2.4 Irradiation Damage of the Ferrite of Stainless Steels

Many of the internal components in a nuclear power plant are made from stainless steel, like 304, 304L, 316, 316L, 321 and 347, welded or clad by alloys 308 and 309, due to the good corrosion resistance at reactor relevant temperatures [65]. These alloys are austenitic, but the welds contain small amounts of ferrite. Just like the low alloy steel in the RPV, these materials are affected by the neutron irradiation during operation. Due to their position closer to the core, the doses can be much higher than for the RPV, up to 100 dpa or more during the operational time of the reactor, dependent on position. Just as in the RPV, the neutrons will interact with the material, creating increased possibilities for diffusion. In austenite, Ni-Si particles (possibly γ', i. e. Ni_3Si and its precursors) are known to form as a result [91–94]. In ferrite, phase decomposition into Cr-rich and Cr-poor volumes occurs (spinodal decomposition), and precipitation of nanometre sized $Mn_6Ni_{16}Si_7$ precipitates known as *G-phase*. The change of microstructure changes the mechanical properties, giving a decreased fracture toughness. In this section, the focus will be on the degradation of the ferrite.

[2] In thermally aged materials, some of the larger "clusters" might be precipitates.

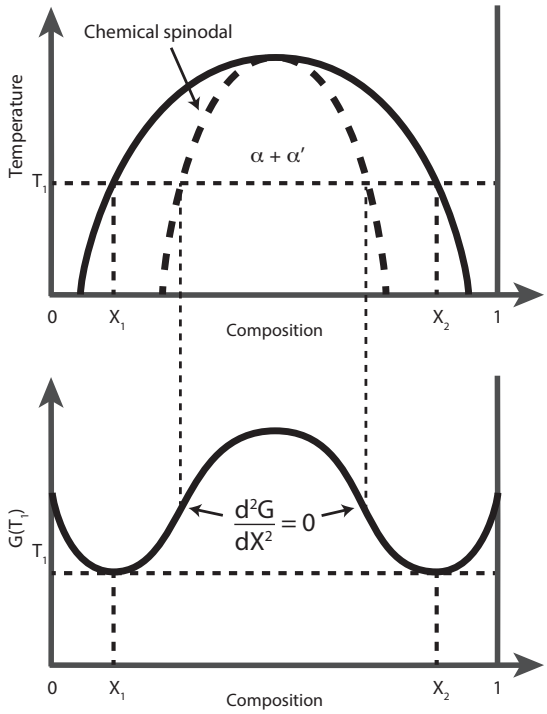

Figure 2.5: Between the spinodals, an alloy will decompose spontaneously. Between the spinodal and the miscibility gap, phase decomposition might happen through classical nucleation and growth.

2.4.1 Theory of Spinodal Decomposition

Spinodal decomposition is a spontaneous phase transformation as there is no barrier to transformation [95]. In a phase diagram such as the one in the upper part of Figure 2.5 there is a miscibility gap where the α and α' phases are stable. Materials go from the single phase above to the miscibility gap during quenching. Inside the spinodal, uphill diffusion will take place as this will decrease Gibb's free energy. The uphill diffusion will continue until the equilibrium compositions X_1 and X_2 are reached (Figure 2.5).

The chemical spinodal is defined as

$$\frac{\mathrm{d}^2 G}{\mathrm{d}X^2} < 0 \tag{2.5}$$

where G is Gibb's free energy and X is the mole fraction of one of the elements. However, it is of little practical use as there are also other factors affecting the spinodal decomposition in a material. Both the chemical difference (different

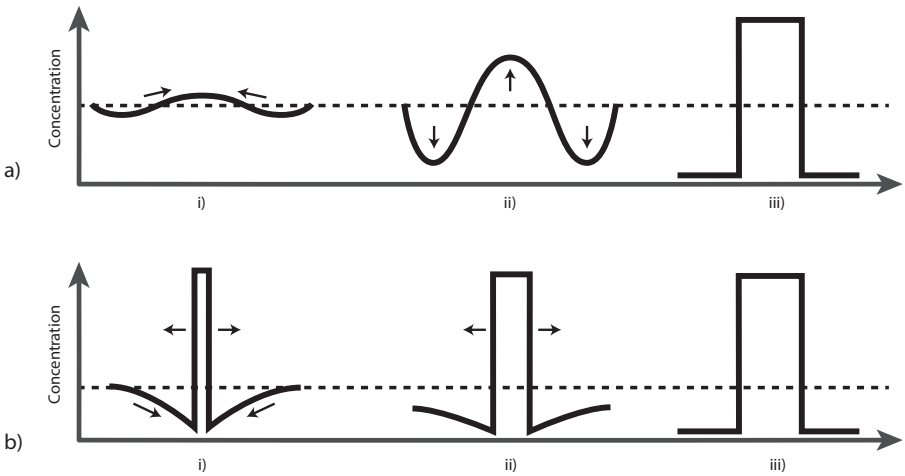

Figure 2.6: A schematic comparison of spinodal decomposition (a) and nucleation and growth outside the spinodal region (b). Time increases from i) to iii).

energies of bonding dependent on which atoms are binding to each other) and the coherency stresses of the phases also affect the decomposition. Thus, those factors are included in the coherent spinodal, saying that decomposition takes place when

$$\frac{\mathrm{d}^2 G}{\mathrm{d}X^2} + \frac{2K}{\lambda^2} + 2\eta^2 E' V_m < 0 \tag{2.6}$$

where the second term describes the bonding difference and the third term the coherency stresses. K is a constant that is dependent on the different bond energies of like and unlike atoms, λ is the wavelength of the spinodal decomposition, $\eta = \frac{1}{a}\frac{\mathrm{d}a}{\mathrm{d}X}$ where a is the lattice parameter, $E' = E/(1-\nu)$ where E is Young's modulus and ν is Poission's ratio. V_m is the molar volume.

The coherent spinodal decomposition has a lower upper temperature limit than the chemical spinodal. The wavelength of the spinodal decomposition has a lower limit given by equation 2.6.

Between the spinodal and the miscibility gap, the phase transformation will take place through nucleation and growth as the alloy is metastable. A comparison of the two possibilities and their effect on compositions can be seen in Figure 2.6.

Spinodal decomposition at early stages can be seen as sinusoidal differences in composition [96],

$$f(x,y,z) = C_0 + A\sin\frac{2\pi(x+y+z)}{\lambda} \tag{2.7}$$

where C_0 is the average composition, A is the amplitude of the decomposition, λ is the wavelength, and x, y and z are the coordinates in the three dimensions. However, at later stages the decomposition will not be symmetrical around the average composition as one phase might reach a minimum content of the other element [97]. The microstructure resulting from spinodal decomposition is in general a complex network of high- and low- concentration volumes.

2.4.2 Spinodal Decomposition in Fe-Cr Alloys

Thermally induced spinodal decomposition in Fe-Cr is known to occur at intermediate temperatures ($300 - 500\,^{\circ}\mathrm{C}$). In ferrite, the Fe-rich phase is known as α and the Cr-rich phase as α' (both phases are bcc). In nuclear power plants, austenitic stainless steels with remaining ferrite in the welds, and duplex stainless steels are used for the internal parts due to their good corrosion resistance, weldability, and mechanical properties. Both the composition of the ferrite of these steels, and the temperatures are in the range where spinodal decomposition occurs, whereas the austenite part is unaffected in absence of irradiation [97, 98]. Both spinodal decomposition in model Fe-Cr alloys and actual alloys have been studied. An increased amount of Cr accelerates the decomposition [99]. In real alloys, the addition of alloying elements (Ni, Si, Mo, Mn,...) is known to affect the decomposition. For instance, Hedström et al. showed that both addition of Ni and Mn accelerate the decomposition of ternary model alloys containing 20% Cr [100].

Adding irradiation gives further complexity to the degradation of the material. The neutrons will interact with the material, creating vacancies and interstitials and increased diffusion, hence making the spontaneous process of spinodal decomposition faster [101, 102]. In this thesis, spinodal decomposition in a neutron irradiated weld from the Spanish reactor José Cabrera (Zorita) is characterised and compared to thermally aged pipe welds from Ringhals R2.

2.4.3 Nucleation of G-phase

G-phase ($Ti_6Ni_{16}Si_7$) is a cubic phase with a lattice parameter four times that of bcc Fe. The Ti in the composition can be replaced by other elements, commonly Mn. The nanometre sized G-phase precipitates were crystallographically identified in the ferrite of thermally aged cast alloy CF8 alloys using TEM by Bentley et al. in 1985 [103]. The ferrite composition affects the formation of the G-phase, for instance Ni, Si, Mo and C are believed to increase the G-phase precipitation [97, 104]. In alloys containing no Mo, G-phase precipitation is only observed at ferrite/austenite boundaries [97].

Nucleation of G-phase exclusively happens at the α - α' boundaries, where the exchange of atoms during the phase separation leads to diffusion of others. The Fe-rich α rejects Ni atoms, and the Cr-rich α' rejects Si, resulting in a total movement of both elements to the boundaries, where they meet and form G-phase together with Mn [97, 105, 106]. Later in this thesis, results on G-phase precipitation are shown in the irradiated core barrels welds from the José Cabrera (Zorita) reactor.

2.4.4 Influence on Mechanical Properties

The spinodal decomposition is found to affect the mechanical properties of ferrite containing steels with high Cr content, due to the strain between Fe-rich and Cr-rich phases, and to lattice friction forces. The result of this is hardness increase and embrittlement. The decomposition is responsible for what is known as the "475 °C embrittlement". The total effect is dependent on the amount, size and distribution of the ferrite in the duplex steel [98].

The influence of G-phase to the hardness of the steel is harder to distinguish, due to the complexity of the system. There are studies that suggest that the G-phase contributes to the hardness [107–109], and other studies that show no or little contribution [110, 111]. There is also a possibility of indirect contribution to the hardening, suggesting that the G-phase contributes to local change in composition (Ni content) and thus the kinetics of the spinodal decomposition is affected [97].

CHAPTER 3

Experimental Techniques

The main experimental characterisation technique used in this thesis is APT. Due to the small size of the clusters of interest, APT is one out of few methods that can be used. Other techniques that are also used for cluster studies in RPV welds are small angle neutron scattering (SANS) (see for instance [112–115]) and transmission electron microscopy (TEM) ([116–118]). SANS enables studies of larger volumes and gives cluster characteristic averages, but needs to be combined with APT for assumptions of cluster compositions. The small cluster size is challenging in TEM, as matrix above and underneath will also contribute to the chemical composition and crystal structures recorded when illuminating a thin lamella with electrons. In this chapter the APT technique and its merits and limitations are described, as well as data analysis for clustering and spinodal decomposition. The chapter is ended with a section on specimen preparation for APT.

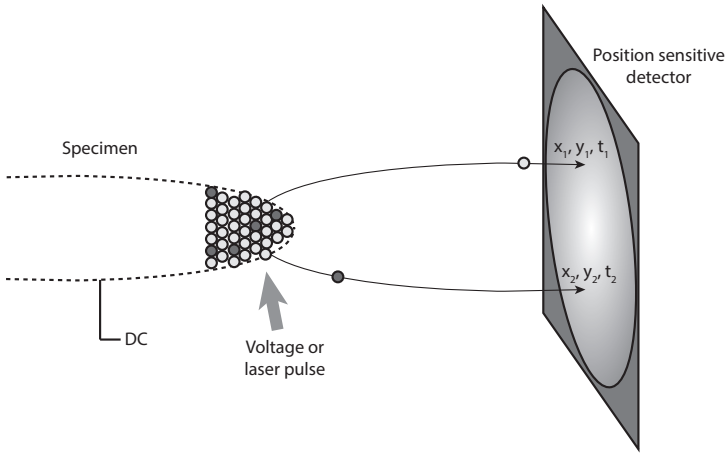

Figure 3.1: Schematic of the experimental setup of APT. Ions are field evaporated by means of a direct current field and laser or voltage pulses. For each ion the time of flight and the position on the detector are recorded.

3.1 Atom Probe Tomography

3.1.1 Overview

Atom probe tomography (APT) is a destructive characterisation technique in which atoms can be identified in terms of both type and position within the specimen. APT is used for detailed material characterisation, with a near-atomic resolution. Common phenomena studied are clustering, segregation to grain boundaries and interfaces, and phase transformations. The technique is well suited for metals that are conducting, but also semiconductors and oxides and even biological materials can be studied. The typical analysed volume is in the order of $50 \times 50 \times 200\,\mathrm{nm}^3$. Unless stated otherwise, the references for this chapter are [119–121].

The basic principle of APT can be seen in Figure 3.1. A needle-shaped specimen in ultra-high vacuum and at low temperatures (typically $30 - 70\,\mathrm{K}$) is subjected to a direct electric field. When the specimen is subjected to a pulse, either voltage or laser, the field might be high enough to ionise and tear off atoms from the apex of the needle in the field evaporation process. The positive ion leaves the specimen surface and hits a position sensitive detector. The time of flight is measured for each ion in order to determine the chemical identity. The information on the position, time of flight and the sequence of ions can be used in order to make a 3D reconstruction of the analysed material. The electric field results in high stresses in the specimen; in fact many APT

analyses are ended by specimen fracture.

3.1.2 Field Evaporation

Field evaporation is the most central process in atom probe analysis. A direct current (DC) voltage is applied to the specimen; the field at the tip is strong, tens of V/nm. If the apex is considered to be smooth and spherical, the electrical field can be described as

$$F = \frac{V}{k_f R} \tag{3.1}$$

where F is the electrical field, V is the voltage, k_f is the field factor and R is the radius of the tip. The field factor is a constant that is dependent on the shape of the tip and the electrostatic environment. A smaller radius of the tip gives a higher field with the same voltage, giving a need of an increased voltage for the same evaporation rate (i. e. number of ions evaporated per pulse) when the radius of the needle is increased during analysis. The penetration depth of the field is very small (for metals less than the size of an atom in the lattice), and hence only atoms at the very surface of the tip are evaporated, atom by atom.

The pulsing is used to overcome the evaporation barrier at a specific, known time. The evaporation is dependent on both the temperature and the electric field. Thus, both voltage pulsing and laser pulsing, effectively meaning heating the specimen, can be used to evaporate the ion, see Figure 3.2. The pulse fraction should be high enough for all elements in the specimen to evaporate, since different elements have different evaporation fields. If the field is not high enough there will be preferential evaporation of the atoms with lower evaporation fields, biasing the composition of the measurement. However, the stresses associated with high fields give a higher probability of specimen fracture that would end the analysis.

3.1.3 Data Reconstruction

In order to make a three dimensional reconstruction of the analysis data, the position of impact on the detector and the sequence of the ions are used for spatial coordinates and the time of flight is used for chemical identification.

The time of flight, the time from the pulse until the ion hits the detector, is recorded during the analysis. The ion leaves the tip surface with zero velocity and is accelerated within a few atomic distances from the tip to the kinetic

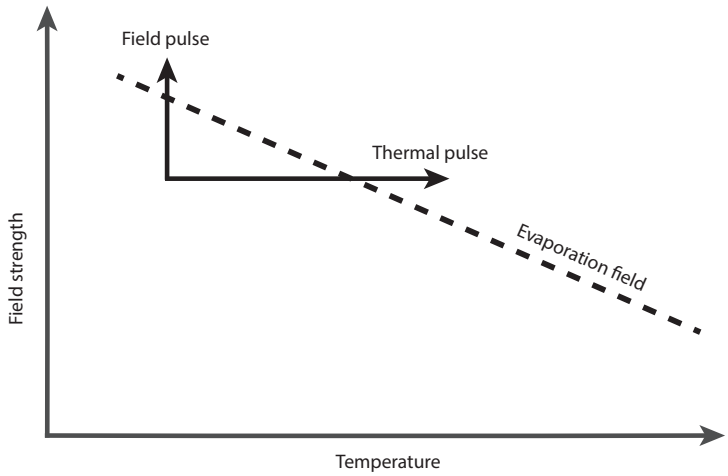

Figure 3.2: Schematic of pulsing and evaporation field. Field pulsing corresponds to voltage pulsing and thermal pulsing to laser pulsing.

energy $E_c = \frac{mv^2}{2}$ where m is the mass and v is the velocity of the ion. The potential energy from the field is $E_p = neV$ where ne is the charge of the ion and V is the voltage. The distance from the tip to the detector, l, is known, and thus the velocity $v = \frac{l}{t_{flight}}$. Combining the three relations gives

$$\frac{m}{n} = 2eV\Big(\frac{t_{flight}}{l}\Big)^2 \tag{3.2}$$

i.e. the mass-to-charge ratio. This ratio is then used for the identification of ions in the mass spectrum, see Figure 3.3. The mass-to-charge ratio detected has some variations, giving widths to the peaks. Therefore, a range is usually given for each ion. For voltage pulsed runs, the width of the peak in the mass spectrum is mainly the result of the extent of the voltage pulse in time. When running analyses in laser pulsed mode, the peaks are often wider and so called thermal tails contribute to the background, due to the transport of heat away from the specimen apex.

The position of the ions in the specimen is reconstructed using the impact position on the detector. The ion trajectories are dependent on the three dimensional field between the tip and the detector, that is dependent on the local environment close to the surface as well as further away. There are some different protocols on how to perform the reconstruction, one commonly used is based on the publication by Bas et al. [122].

The choice of reconstruction parameters is vital, if they are not properly chosen distances and shapes in the reconstruction will be distorted. The analysed volume might get compressed or elongated. For the reconstruction both the field

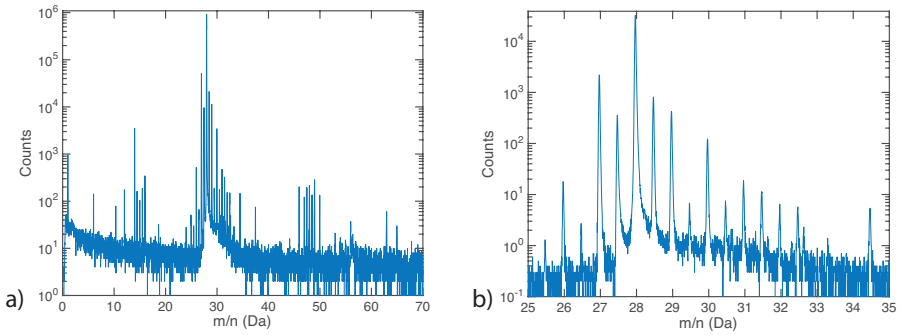

Figure 3.3: Example of a spectrum from a voltage pulsed analysis for ion identification. This material is the Ringhals R4 weld. a) Full spectrum. b) Enlarged part of the spectrum from 25 to 35 Da. The peak at 28 Da corresponds to $^{56}Fe^{++}$ that is the most abundant ion in the analysis. The binning of the histograms are different in a) and b).

F and the shape of the apex dependent field factor k_f are needed. Also, the image compression factor is needed. The image compression factor describes the ratio between the crystallographic angle and the observed angle,

$$\xi = \frac{\theta_{crys}}{\theta_{obs}} \tag{3.3}$$

and can be calibrated using the crystallographic information from the detector hit map, namely the distances between poles with known plane distances and the usage of $\theta_{obs} = arctan\frac{D}{L}$ where D is the distance to the detector and L is the distance in the hit map (the simplification is possible since the specimen tip has a negligible radius compared to D). There are some different ways of estimating the shape of the specimen for determination of the field factor k_f. Equation (3.1) can be used with a knowledge of the evaporation field for the material analysed, connecting to the voltage. The radius could be determined by TEM, beneficial if there are different phases with different evaporation fields in the analysis. One way of knowing if the parameters are correct is by evaluation of the atomic planes at crystallographic poles. The analysis of the poles gives high quality data in the direction of analysis in some materials, such as low alloy steel. Known features could also be used for finding reconstruction parameters; for instance precipitates growing with certain angles or in certain shapes.

3.1.4 Statistical Tools and Cluster Algorithms

Once the reconstruction is performed there are literally millions of data points. In this section, some statistical methods and some cluster analysis methods are briefly described. Note that the words cluster and precipitate are used interchangeably.

The radial distribution function (RDF), is also known as the pair correlation function and denoted $g(r)$. It describes the normalised probability of finding other atoms of the same species at a distance r from the reference atom. It can be related to the number density $\rho(r)$ and average number density $\rho_{av}(r)$ of atoms by

$$g(r) = \frac{\rho(r)}{\rho_{av}(r)} \tag{3.4}$$

When $g(r)$ is larger than unity for small distances, there is clustering of the specific element(s) studied.

Isoconcentration surfaces can be used to illustrate clusters as well as other features such as layers, grain boundaries and line dislocations [120]. The surface is defined at a specific concentration of an element. These surfaces can also be used to create proximity histograms, proxigrams, where the concentration of different elements is shown as a function of the distance from the surface [123]. For small precipitates proxigrams might give poor statistics on the inside of the surface due to the small number of atoms.

The maximum separation method (MSM) is a method that utilises the distance between solute atoms to identify clusters [35, 124, 125]. Two solute atoms are considered being within the same cluster if they are closer to each other than a distance d_{max}, see Figure 3.4. A smallest number of atoms considered being a cluster, N_{min} can be chosen in order for random fluctuations in the matrix not to be considered as clusters. A higher order, N, than one (the nearest neighbour), can be set, meaning that the N:th nearest neighbour is considered. In order to determine cluster composition, a parameter L (envelope distance) can be chosen in order to include other atoms than the solute ones used for cluster identification. L is the distance from the solute atoms that is considered being part of the cluster. In order to get rid of the matrix atom halo, another distance E, the erosion distance, can be used to remove atoms from the cluster surface. There are other methods of detecting clusters, see reference [64] for a review.

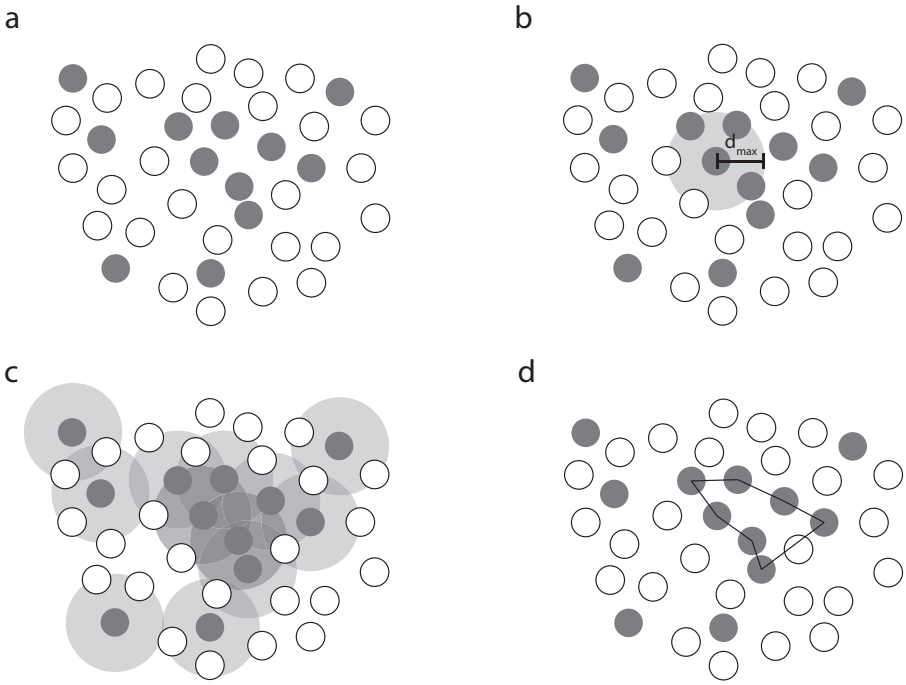

Figure 3.4: Schematic of the MSM. a) Solute atoms (filled) in the matrix (white atoms). b) Atoms within the distance d_{max} from a solute atom might be part of the same cluster. c) The vicinity of all solute atoms are checked. d) Atoms identified as being in the same cluster are marked with a line.

3.1.5 Evaluation of Spinodal Decomposition

APT is a useful technique when interested in finding the wavelength and amplitude of spinodal decomposition, as described in equation 2.7. One commonly used method is the Langer-Bar-on-Miller (LBM) method [121, 126], where two Gaussian distributions are fitted to the frequency distribution of Cr, and the amplitude of the spinodal decomposition is taken as the difference in Cr average content between the distributions. The results obtained by this method are dependent on block size (commonly 33, 50 or 100), that is determined by the user.

In this thesis, another method developed by Zhou et al., based on the RDF (equation 3.4) is used [127]. Assuming sinusoidal variation in Cr concentration (equation 2.7), the amplitude A of the decomposition will be connected with the normalised and extrapolated Cr RDF at zero distance as

$$A = C_0\sqrt{2(RDF(0) - 1)} \tag{3.5}$$

where C_0 is the average Cr content. The wavelength of the spinodal decomposition can be determined by the local maximum of the RDF of Cr (corresponding to many Cr atoms having another Cr atom at that specific distance). This method has the benefit of being user independent. The limitation in this method lays in the assumption of a sinusoidal variation in composition; this is probably true for early stages of decomposition. However, as the process evolves, the lower limit of one of the phase contents might be reached. What then happens is that the size of the volumes of the two phases will be different, and the decomposition will no longer be sinusoidal. Furthermore, it is also possible that the interface between the phases will get sharper when the decomposition evolves, and thus it will evolve towards a compositional profile more similar to a square wave.

3.1.6 Limitations

Even though APT is a powerful technique there are certain limitations. First of all, it is not possible to analyse any material. The implementation of laser pulsing in APT made it possible to expand from analyses of conductive materials only to semiconductors, minerals, biological materials and more. However, many materials prove hard to analyse due to uneven evaporation, and early specimen fracture. This limitation does not concern the steels analysed in this work, that runs well in the APT as they are conductive and have suitable mechanical properties.

An issue for atom identification is peak overlap, two isotopes having the same mass-to-charge ratio. The overall composition of the analysis could generally

be obtained by deconvolution of the peaks since the other isotopes of the same element can be used together with the known natural isotope abundance. However, the identity of each individual atom is still unknown. In some cases, the amount of overlap is very high, for instance in analyses of oxides with many molecular ions, or polymers, containing hydrides that make ranging of the spectrum a true challenge. In steels such as the RPV welds, the $^{28}Si^{++}/^{14}N^{+}$ overlap makes quantification of nitrogen hard. There is also an overlap for $^{58}Ni/^{58}Fe$, making the cluster interfaces of NiMnSi-rich clusters more diffuse. Furthermore, aluminium only has one naturally occurring isotope, that comes as $^{27}Al^{+}$, overlapping with $^{54}Fe^{++}$ when laser pulsed analyses of steel are conducted.

The spatial resolution is almost atomic, but it is not perfect. Crystallographic planes can only be detected in some fairly pure materials and even then only at crystallographic poles. For some materials and atomic species there is surface migration prior to field evaporation, giving the reconstruction a dependence of the crystallography [128, 129]. The issue is more pronounced when using laser pulsing. One example of this redistribution is Si in low alloy steels.

Different evaporation fields of different phases alter the evaporation sequence, resulting in the so called local magnification effect [130, 131]. Hence, for instance a cluster containing a high evaporation field element will evaporate later than the surrounding matrix. The cluster will form a small protrusion on the tip surface, with another radius than the full tip, and thus the trajectories of the cluster ions are affected, making the cluster appear diluted by matrix atoms. If the evaporation field of the cluster is lower, then an area with a larger local radius will form in the needle surface, also affecting the ion trajectories. In the case of the clusters in RPV steels, this has generated discussion on the true Fe content of the clusters, since APT analysis generally gives a composition of around 50% Fe. Studies have shown that the Fe content of the clusters probably is considerably lower [116, 132–134]. A sign of this phenomenon is an unphysically high atomic density within the clusters in the reconstruction, since the clusters have a low evaporation field, especially for Cu-rich clusters. The exact Fe content is unknown, and when evaluating cluster composition and size, the assumptions on the Fe content made need to be mentioned.

Another consequence of the different evaporation fields of different phases is that the reconstruction of an analysis made over two or more phases might be hard to perform as the reconstruction parameters thus might vary in the same analysis. For instance, some carbides in metal matrixes will appear to have a lower atomic density; something that they do not have in reality. Furthermore, carbides are hard to analyse due to C atoms evaporating as cascades. Due to the detector having a dead time, the carbon content is then underestimated [135].

3.2 Specimen Preparation Methods

There are some requirements on the APT specimen. The specimen needs to be in the shape of a needle, and the tip radius of curvature should be around 50-150 nm in order to create fields high enough for evaporation at voltages of operation in the atom probe (usually 2-10 kV). The cross-section of the needle needs to be circular in order for the reconstruction to be accurate. The feature of interest needs to be close enough to the specimen tip (around 100 nm) in order to be captured in the analysis. The surface of the specimen should be smooth and free from protrusions and cracks that might increase the risk of fracture and make the reconstruction less like the specimen. The taper angle of the needle should be small for obtaining long runs, but very long and thin needles might have a higher risk of fracture. Typically, the angle is around 5°. Also, there should be no secondary tips close to the tip of interest that might field evaporate and contribute to the signal. These requirements can be fulfilled using electropolishing or doing a focused ion beam/scanning electron microscope (FIB/SEM) lift-out that is described below.

3.2.1 Electropolishing

Electropolishing is a convenient, fast and cheap method for specimen preparation of electrically conducting materials. In order for the cross section of the resulting needle to be circular the cross section of the starting blank needs to be either circular or square. Common measures are $0.3 \times 0.3\,\mathrm{mm}^2$, with a length of around 15 mm. Two needles can be produced from the same blank. The blanks need to be cut without introducing any stress or heat that might change the microstructure of the material, making a low speed saw with cooler/lubricant one alternative.

The electropolishing can be done in different ways, but the principle is the same. Here a two-step double layer technique is described, see Figure 3.5. The idea is to create a necked specimen in the first step, in a high concentration electrolyte. The very sharp tips are created in the second step in a dilute electrolyte in a controlled way. In the first step, a thin layer (a couple of mm) of a high concentration electrolyte is put on top of a dense, inert liquid such as polyflourinated polyether or Galden®. The blank (anode) is hung in this liquid so that the middle of the blank is in the electrolyte. There is also a counter electrode (cathode), in the shape of a loop or a stick, in the electrolyte. The counter electrode is made from a noble metal such as Au or Pt. When a voltage is applied the specimen is polished in the electrolyte region. The blank could be moved up and down in order to avoid reactions at the electrolyte - air interface (crucial at high air humidity) and in order to get a smaller taper angle. When there is a necked region with a small

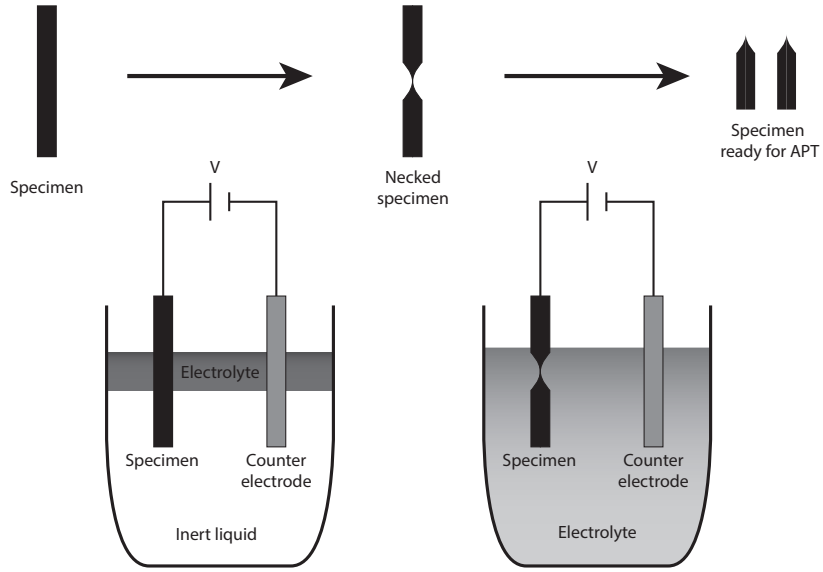

Figure 3.5: The two-step electropolishing procedure. A neck is etched in the first step. In the second step the blank is further etched until two specimens are created.

radius the specimen can be moved to a low concentration electrolyte. The electropolishing is continued until the neck no longer can support the weight of the lower part of the blank and it drops to the bottom of the electrolyte. The switching off can be automated by turning off the voltage when the current drops due to the smaller anode after dropping half of the blank. The lower part of the blank can also be used as a specimen. If needed, the specimens can be subjected to some pulsed electropolishing to get rid of surface oxides after this step. They can also be examined in the optical microscope or even in the scanning electron microscope (SEM) or TEM, or FIB/SEM and further oxides can be removed by Ga-ion milling if needed. The choice of electrolyte and voltage for the different steps is dependent on the material, see Table 2.1 in [119] for a summary.

3.2.2 FIB/SEM Lift-out Technique

Focused ion beam/scanning electron microscopy (FIB/SEM) can also be used for making APT specimen. The microscope is equipped with both an electron column and an ion column, at an angle (52° in an FEI Versa for instance), see Figure 3.6. Both the electron beam and the ion beam can be used for imaging and depositing an other element, for instance Pt. The ion beam can also be used for milling material in a highly controlled manner. Site specific

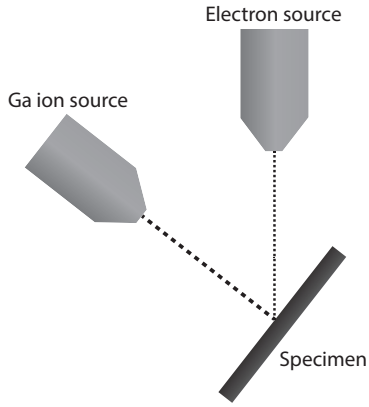

Figure 3.6: Schematic of the FIB/SEM.

regions can be lifted out if there is a feature of interest, for instance a grain boundary. The volume of the material needed is small, that could be beneficial for instance if the material is slightly radioactive and small volumes of material are preferred.

There are different ways of making a lift-out depending on the material, and the position of the feature of interest. Here, a standard lift-out finalised with annular milling [136, 137] is described, that can be used for site-specific specimen preparation from bulk material. First, a site of interest is chosen. A layer of Pt is deposited in the shape of a square, see Figure 3.7. The area of the square is typically in the order of $25 \times 2\,\mu\text{m}^2$. Then, a high ion beam current is used to cut along the long edges of the deposited area, with an angle of 30° to the surface of the bulk specimen. The width of the cuts needs to be enough to avoid redeposition of the milled material reconnecting the lift-out with the bulk. One of the short edges is cut loose. Then, a micromanipulator is attached to the end of the bar using Pt deposition. The other end of the lift-out is cut with the ion beam. Then, the wedge can be lifted out from the bulk. The specimen can be placed on some different types of holders, for instance a prepared TEM-half-grid for correlative microscopy or a prefabricated Si-post coupon (as in the figure). The specimen is attached on one side of the wedge and then cut free using Ga ions. The process is continued for as many specimens as are needed or until the bar is consumed. The Si posts are rotated and Pt is deposited on the other side as well. The specimen can then be sharpened using annular milling. The milling is commenced with large inner and outer radii and a high ion beam current. Successively, the radii and current are decreased until the needle is sharp and located in the position of interest. The final step is a short milling session with low voltage and current in order to get rid of ion beam damage, i. e. the amorphous surface layer, and Ga implantation from the milling.

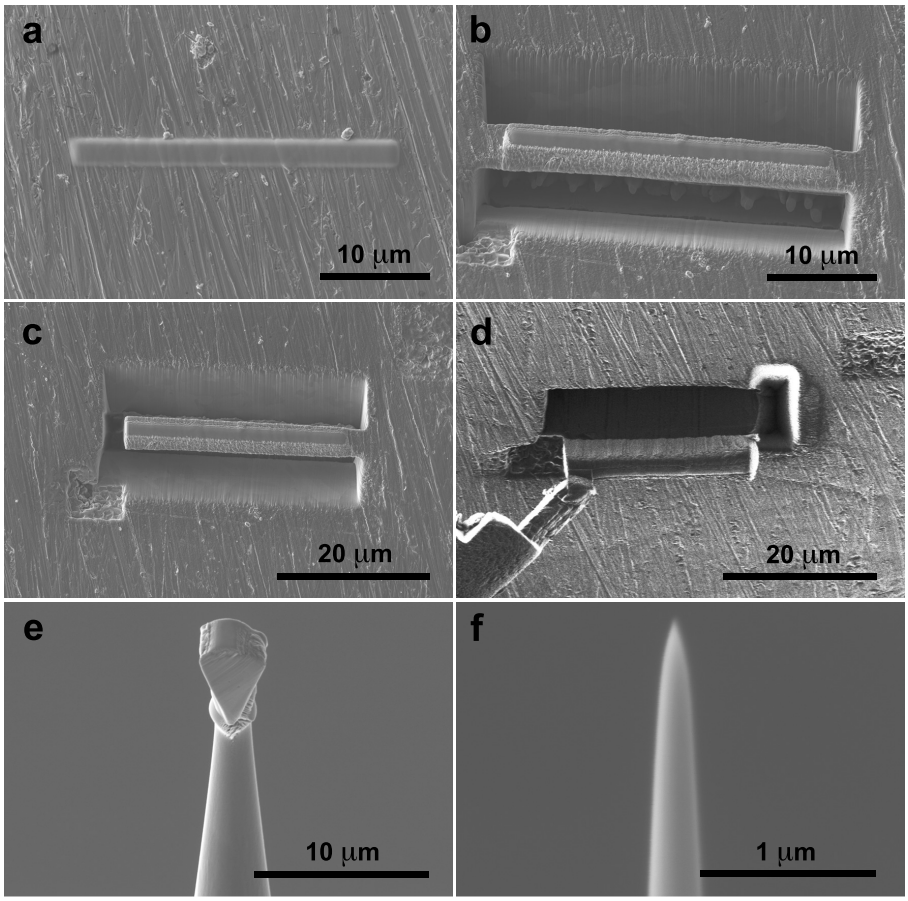

Figure 3.7: Liftout procedure. a) Pt deposition on the site of interest. b) Trenches are milled on both sides of the Pt strip. c) One side of the volume of interest is cut. d) The volume of interest is attached to the micromanipulator, cut on the other side and lifted out. e) A piece of the lift-out is attached to a Si post. f) The specimen is sharpened using annular milling, ready for analysis in the atom probe.

CHAPTER 4

Materials

Three main sets of weld metals were analysed; the irradiated Ringhals R4 reactor pressure vessel steel surveillance and Halden irradiated materials in *Papers I*, *II*, *IV*, and *V*, the thermally aged Ringhals R4 pressurizer in *Papers III* and *IV*, and the core barrel material from the Zorita nuclear power plant in *Paper VI*.

4.1 Ringhals R4 Reactor Pressure Vessel

The materials studied are identical to the RPV welds in Ringhals R4. R4 is a PWR commissioned in November 1983, designed by Westinghouse Electric Company [6, 138]. The composition of the RPV welds can be seen in Table 4.1. The welds are high in Ni and Mn, and low in Cu, compared to other reactors worldwide. The RPV itself was fabricated by Uddcomb using SA 508 class 2 Klöckner Werke ring forgings. The welding was done by SAW with a PWHT at 620 °C in order to relieve internal stresses. The surveillance blocks were supplied by the same company, produced in accordance to the same welding procedure specification (WPS).

The welds consist of mainly bainite. The general microstructure of the weld

Table 4.1: Composition of Ringhals R4 RPV weld metal. Fe balance [6].

	Cu	Ni	Mn	Mo	Si	C	P	S	Cr	Al	Co
at.%	0.04	1.58	1.37	0.29	0.28	0.31	0.027	0.007	0.04	0.05	0.01
wt.%	0.05	1.66	1.35	0.50	0.14	0.068	0.015	0.004	0.04	0.024	0.01

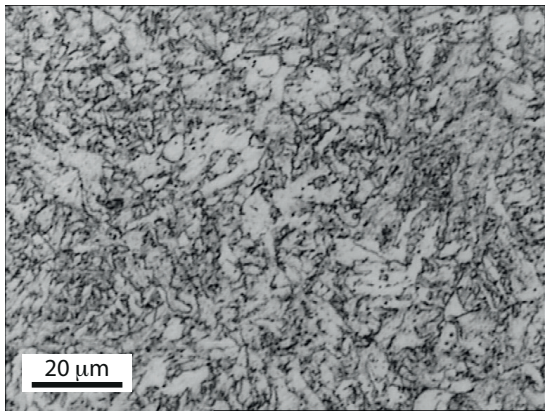

Figure 4.1: Microstructure of the RPV weld metal imaged using a light optical microscope.

is shown in Figure 4.1.

In Table 4.2, the fluence and flux for the four studied materials can be seen. One unirradiated reference material has been studied, as well as two materials irradiated in the OECD Halden Materials Test Reactor in high flux, and one surveillance material irradiated inside the RPV of R4. The difference in flux between the Halden irradiated materials and the surveillance material is around 20 times. The lead factor of the surveillance material is around 3, i. e. the surveillance material flux is around 3 times higher than the flux experienced by the R4 RPV. The irradiation temperature of the Halden irradiated materials was $290 - 295\,^{\circ}\mathrm{C}$. The surveillance material was irradiated inside the reactor, the temperature was $284\,^{\circ}\mathrm{C}$. The main neutron irradiation spectrum differences between Halden and Ringhals is for the low energy neutrons ($0.1 - 1\,\mathrm{eV}$) that do not influence the material damage [8, 67].

Table 4.2: Irradiation fluence and flux. H refers to materials irradiated in Halden, S refers to surveillance material.

Name	Fluence ($10^{23}\,\mathrm{n/m^2}$)	Flux $10^{16}\,\mathrm{n/m^2 s}$)
Reference	0	-
H2.0	2.0	2.3
H6.4	6.4	3.8
S4.6	4.6	0.15

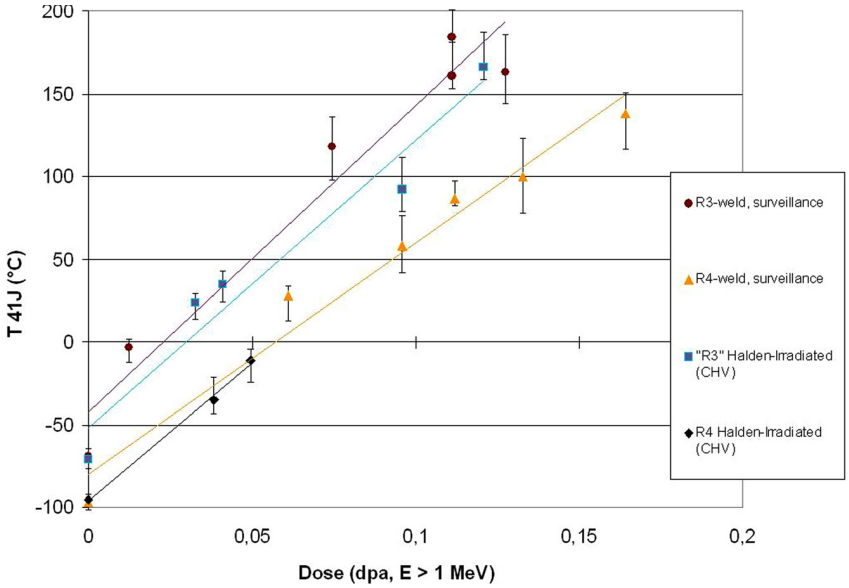

Figure 4.2: The transition temperature from Charpy V testing (CHV) for different doses of the Ringhals R3 and R4 surveillance material and the material irradiated in Halden. Reproduced, with permission from [8], copyright ASTM International, 100 Barr Harbor Drive, West Conshohocken, PA 19428.

The beginning of life DBTT for Ringhals R4 welds was quite low, $-75\,^{\circ}\mathrm{C}$ [6]. The influence of the dose on the DBTT for the surveillance material of R4 can be seen in Figure 4.2. The shift is unexpectedly high, $162\,^{\circ}\mathrm{C}$ for a fluence of $6 \cdot 10^{23}\,\mathrm{n/m^2}$ [6]. The large shift is generally attributed to the high Ni and Mn content of the welds. The surveillance material of Ringhals R3 and R4 has been analysed using APT by Miller et al. [52] and Styman et al. [80]. They found a high number density (around $4 \cdot 10^{23}\,/\mathrm{m^3}$) of nanometre sized clusters containing Ni, Mn, Si, and some Cu. Styman et al. also performed post irradiation annealing on the R3 welds to study the cluster dissolution. Cluster dissolution started after annealing 30 min at $450\,^{\circ}\mathrm{C}$, led by Mn atoms, and continued during further annealing at $500\,^{\circ}\mathrm{C}$. The hardness was recovered with the clusters dissolving. Furthermore, Hyde et al. studied the Ringhals R3 surveillance materials using SANS [139]. The results were consistent with the results from APT, and the combination with simulations also showed that features that are unresolvable in the experiment should not significantly impact the total volume fraction of features.

The mechanical properties of the Halden irradiated materials are described in [8, 140]. What was found was that even though there is a significant difference in flux between the surveillance material and the material irradiated

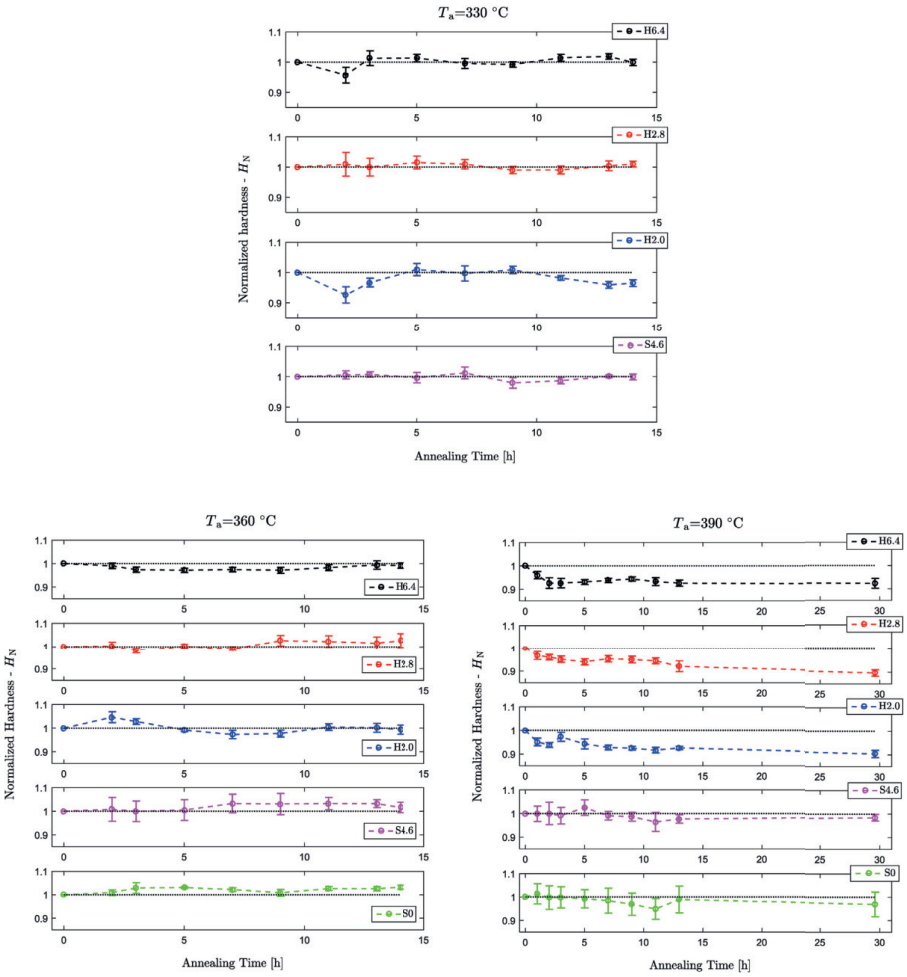

Figure 4.3: Relative hardness after annealing the RPV weld metals at 330 °C, 360 °C, and 390 °C. Reprinted from Journal of Nuclear Materials, 484, Boåsen, M., Efsing, P., Ehrnstén, U., On flux effects in a low alloy steel from a Swedish reactor pressure vessel, 110-119, Copyright (2018), with permission from Elsevier.

in Halden, the change in mechanical properties (DBTT, see Figure 4.2, and hardness) shows the same dependence on fluence [8]. However, a difference in hardness could be seen during the initial hours when annealing the materials at a temperature of 390 °C, when the hardness of the high flux materials decreased by a few percent (but not back to the hardness of the reference material), whereas the surveillance material kept the same hardness, see Figure 4.3 [140]. The difference was tentatively attributed to small clusters in the high flux material dissolving, but is further discussed in the results section in this thesis and in *Paper V*.

4.2 Ringhals R4 Pressurizer

In 2011, the pressurizer of Ringhals R4 was removed and replaced during outage. The base metal is of the type A533 Grade B Class 1, welded by Uddcomb, and thus having the characteristic high Ni and high Mn, and low Cu content in the welds, just as the Ringhals R4 RPV. A stress relief treatment at 620 °C was done after welding. The analysed welds were in operation for 28 years at 345 °C. Two different welds were analysed, one circumferential (W1), where the outer SAW welded part was analysed, and the inner part was welded by manual metal arc welding due to space limitation during fabrication. The second weld, W2, is vertical and SAW welded through the entire thickness. Both welds can be seen in Figure 4.4. The check-in transition temperature for the outer part of W1 was reported to be −51 °C, and the yield stress 579 MPa. Boåsen et al. performed mechanical testing on W1 after 28 years of operation, measuring a yield strength of 656 MPa, i. e. an increase of 77 MPa [141]. In *Paper III* and *IV*, studies of the W2 weld are presented.

4.3 José Cabrera Core Barrel and Ringhals R2 Internals

The nuclear power station José Cabrera in Almonacid de Zorita, outside Madrid in Spain, was decommissioned in 2006. The commissioning was in 1968. The core barrel of the Zorita power plant consists of stainless steel 304 plates. In this work, the welds (type 308) have been analysed. The welds contain $5 - 7$ % of ferrite (as measured by ferritescope) [142, 143]. The small volume of ferrite can also be seen in the SEM image in Figure 4.5. The typical width of the ferrite is around 200 nm, making specimen preparation using FIB/SEM necessary for APT specimen containing ferrite.

In Table 4.3 the ageing conditions are given. The samples CB-0.15, CB-1 and CB-2 come from different positions of the core barrel, being exposed to different flux during the life-time of the reactor. Initially, the CB-0.15 material was chosen to be the reference of a low-dose material. However, it was found that

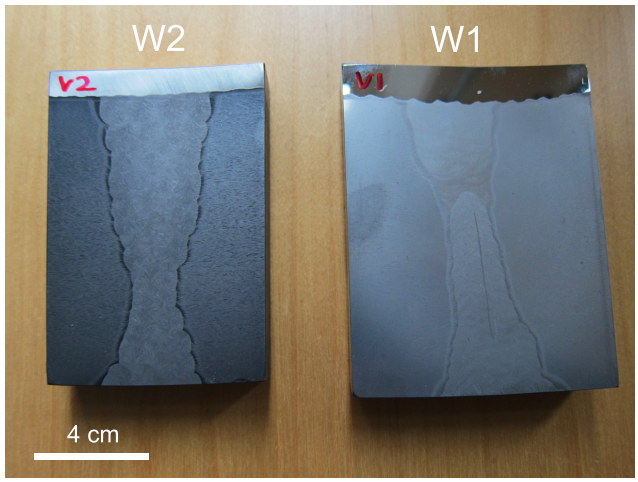

Figure 4.4: The pressurizer welds W1 and W2.

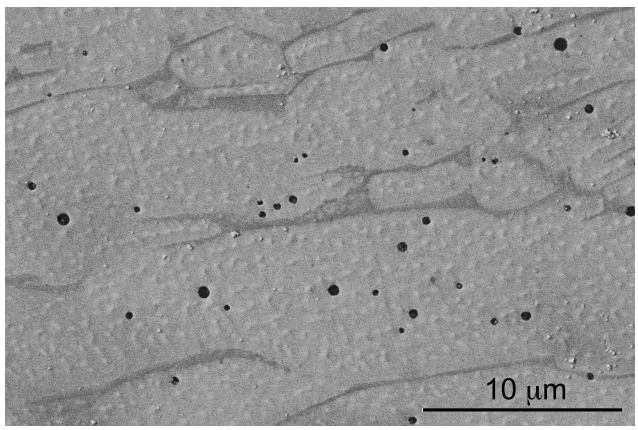

Figure 4.5: Scanning electron micrograph of core barrel weld.

Table 4.3: Irradiation fluence and temperatures of the core barrel (CB) and reference material welds.

Name	Dose (dpa)	Temperature (°C)	Time (h)
CB-0.15	0.15	280-285	231,000
CB-1	1	280-285	231,000
CB-2	2	280-285	231,000
CL	0	291 (274)	70,000 (22,000)
HL	0	325 (303)	70,000 (22,000)

the degradation of this material was well developed already after 0.15 dpa, and thus a hot leg (HL) weld and a crossover leg (CL) weld that had not been exposed to neutrons were introduced as references. These welds originate from the PWR Ringhals R2 internals, a 308 type weld used for CF8M cast components [143]. After initial ageing for 70,000 h, both CL and HL were further aged at lower temperatures for 22,000 h (also in-reactor). The HL material is less relevant than the CL material, as the temperature is significantly higher, more than compensating for the shorter ageing time [144].

The overall nominal composition of the Zorita materials and the HL and CL is expected to be similar [143, 145]. However, HL and CL have a significantly higher ferrite Ni content than the irradiated materials. This could be due to an overall difference in composition, or due to a slower cooling rate during manufacturing of CL and HL, making the Ni partition from the austenite to a higher extent. All the materials in Table 4.3 are further discussed in *Paper VI*.

CHAPTER 5

Summary of Results

In this chapter, the results of the appended papers are summarised and shortly discussed in relation to each other. First, *Paper I* is described. It contains details on the evaluation method of the clustering in the Ringhals RPV welds. This is needed for the cluster analysis in the following papers. In *Paper II*, the viability of using MTRs with higher neutron flux in order to predict the clustering of NiMnSi-rich clusters is described. This is discussed in relation to *Paper V*, where the presence of irradiation induced matrix defects, and the effect of flux, in the Ringhals R4 RPV welds are discussed, as well as cluster dissolution during post irradiation annealing (PIA). *Paper III* brings up the topic of thermal ageing in the former pressurizer of Ringhals. In *Paper IV*, the clusters formed from irradiation and thermal ageing are compared. Finally, this chapter is concluded with results from *Paper VI*, where the spinodal decomposition and G-phase formation in the José Cabrera (Zorita) core barrel welds are characterised.

5.1 Analysis of Irradiated Materials using APT

The analysis of irradiation induced clusters in RPV steels is a challenge. There are two steps from the actual material to the results; first of all, the resolution

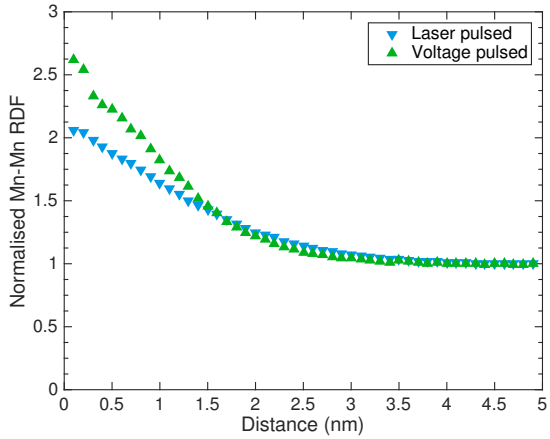

Figure 5.1: Normalised Mn-Mn radial distribution functions for a laser pulsed analysis and a voltage pulsed analysis of material H6.4. Data from *Paper I* [146] replotted.

of the APT, which is affected by the field evaporation phenomena and local magnification effects (matrix atoms end up inside the clusters due to the difference in field). This, together with the less than 100% detection efficiency of the instrument, makes the clusters appear more diffuse in the APT data than they were in the material. Some surface diffusion may occur prior to evaporation, and furthermore there might be local magnification effects due to the crystallography. Collapsing atomic planes, giving an increased number of multiple events, result in evaporation between the pulses, and thus atoms are not detected. All of these phenomena result in volumes with high or low density, dependent on the crystallography of the evaporating surface. P and Si are strongly affected by surface diffusion, but also other elements appear heterogeneously distributed, such as the clustering elements Ni and Mn. This effect is larger for laser pulsed analysis than for voltage pulsed analysis. The RDF of Mn-Mn in the irradiated Ringhals R4 material is shown in Figure 5.1 to illustrate this. A high RDF value for small distances indicates a more well-defined clustering. In addition to this, the definition of a cluster, or the cluster algorithm and parameters, need to be defined in a way that differentiates the clusters from random matrix fluctuations. In the case of the Ringhals R4 materials, the material is both high in Ni and Mn, and thus, the clusters consist of mainly Ni and Mn, making them suitable elements for cluster identification. However, there is still a considerable amount of Ni in the matrix, complicating cluster identification as it decreases the relative contrast.

In *Paper I*, MSM (see Chapter 3.1.4) is used to identify clusters in the high flux irradiated Ringhals R4 welds. Suitable solute atoms for cluster definitions were found to be Ni (29 Da peak excluded due to the overlap with $^{58}Fe^{++}$), and Mn, and in the case of voltage pulsed analyses, Si. Using Cu only would

give more well-defined clusters when analysing RDFs, but would on the other hand give different cluster compositions as the Cu is not evenly distributed within the clusters, and thus the results would be less representative. Using Cu in addition to Ni and Mn gave a negligible improvement due to the low Cu content. Suitable parameters were found through various methods, which were giving similar results. For the irradiated Ringhals welds, a $d_{max} = 0.5\,\text{nm}$ and $N_{min} = 18$ are reasonable choices.

MSM could be used with first nearest neighbour (order=1) or considering higher orders of neighbours. When comparing the first order and eight order (with a different optimised d_{max}) in the H2.0 material containing small and diffuse clusters, it was found that the eigth order require higher N_{min} values, and thus the smallest clusters could not be detected in this material. Therefore, the first order was used (which is also the most common choice in literature).

A sensitivity analysis was made to show how much the parameter choice affects the cluster analysis. The larger and more well-defined clusters in material H6.4 (Table 4.2) were, as expected, less affected by small changes in clustering parameters. Changing $d_{max} \pm 0.05\,\text{nm}$ and $N_{min} \pm 2$, that are within a reasonable parameter range, the number density decreased by 7% or increased by 5%, i. e. the changes are small. The same analysis for material H2.0, which contains smaller clusters, the decrease was 35% and the increase 26%, showing that the results are very sensitive to the exact choice of parameters, due to the nature of the APT data.

5.2 Effects of Neutron Fluence and Flux on RPV Weld Metal

In *Paper II*, the clusters formed in surveillance material (lead factor of around 3) were compared with high flux MTR irradiated materials (lead factor of 45-75) with different fluence, see Table 4.2. In all materials, clusters containing mostly Ni and Mn, but also Si and Cu were formed during neutron irradiation. The clusters were found evenly distributed in the matrix, and also on dislocations, see Figure 5.2. By comparing the high flux materials H2.0 and H6.4, the effect of fluence can be studied. The cluster number density increases fast when the irradiation is commenced and up to $2.0 \cdot 10^{23}\,\text{n/m}^2$ (material H2.0, with number density of around $4.3 \cdot 10^{23}\,\text{clusters/m}^3$, see Table 5.1). In material H6.4 (irradiated to $6.4 \cdot 10^{23}\,\text{n/m}^2$), the number density of clusters is slightly higher, in average around $6.6 \cdot 10^{23}\,\text{clusters/m}^3$, but the rate of the increase has decreased. In comparison, the surveillance material S4.6 has a lower number density than material H2.0, so clearly the cluster number density depends on flux.

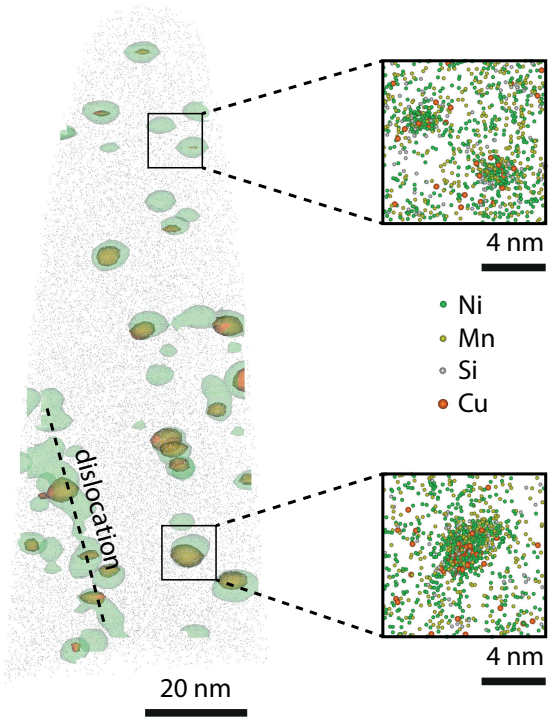

Figure 5.2: Reconstruction of APT analysis, material H6.4. Green surfaces correspond to 5 at.% Ni+Mn+Si, and orange surfaces to 1.2 at.% Cu. The boxes show all Ni, Mn, Si, and Cu atoms within two volumes of $10 \times 10 \times 10\,\mathrm{nm}^3$. Figure from *Paper II* [147].

Table 5.1: The number densities and average diameters after irradiation.

Name	Average number density (10^{23} clusters/m^3)	Average diameter (nm)
Reference	0	-
H2.0	4.3	1.5
H6.4	6.6	1.8
S4.6	3.1	2.5

The size distributions of the clusters are also affected by the neutron fluence and flux, see Table 5.1. The average size of clusters grows from 1.5 nm in H2.0 to 1.8 nm in H6.4. There is a clear flux effect as the cluster diameter of S4.6 is considerably larger (2.5 nm in diameter) although the fluence is lower than for H6.4. There are no signs of so called *late blooming phases*, a sudden increase in clustering after longer times.

Earlier studies of mechanical properties [8] (Figure 4.2) have shown no influence of flux for the Ringhals welds. The welds irradiated in high flux in Halden follow the same trend regarding hardness increase and DBTTs as the surveillance material. However, the high flux materials contain a higher number density of smaller clusters than the surveillance material, compensating for each other in terms of effect on embrittlement. It was found that the dispersed barrier hardening model (see Chapter 2.2.4) with a fitted $\alpha = 0.15$ described the hardness increase based on the cluster characteristics obtained.

The composition of the clusters was similar in all irradiated materials, with small effects of the fluence and flux. It was, however, interesting to find that the size difference between the high flux materials and the surveillance material was mostly explained by an increased number of Ni, Mn and Si atoms in the clusters, whereas the number of Cu atoms was similar. The possibility of formation of phases such as Γ_2 (Ni_3Mn_2Si) and G-phase ($Ni_{16}Mn_6Si_7$) was discussed, but no conclusions on a possible phase transformation could be made based on the current data. The compositions of the clusters did not match any of these two phases.

Annealing studies of the H6.4 weld are presented in *Paper V*. The high flux material was analysed using APT after annealing at 390 °C, 405 °C, 420 °C and 450 °C for 24-30 h. Earlier hardness measurements (Figure 4.3, [140]) show an initial decrease in hardness after annealing at 390 °C for the high flux material H6.4, but not for the surveillance material S4.6. An initial hypothesis of this being due to faster cluster dissolution was turned down as there is no barrier for cluster dissolution, and no difference in cluster characteristics were found before and after annealing at 390 °C. A possible explanation is the presence of matrix defects that are stable at reactor temperatures, but dissolved at 390 °C, which are formed due to the effect of the higher flux. Assuming this, and thus removing their contribution to the hardness, the dispersed barrier hardening

model α parameter is fitted to 0.12, that is also within the interval found in RPV welds in literature [78]. Thus, the hardness contribution of possible matrix defects is small in comparison to the contribution from the clusters in the high flux MTR irradiated material.

At 405 °C, the cluster dissolution starts, by a strongly decreased cluster number density, and a change in cluster composition. Ni, Mn and Si atoms leave the clusters. The remaining clusters are slightly smaller than the original clusters, but contain more Cu atoms, i. e. there is a coarsening process with respect to Cu taking place at 405 °C. The remaining clusters are sitting on dislocations to a larger extent than the initial clusters. Annealing at even higher temperatures further reduces the cluster number density. After annealing for 24 h at 450 °C only a small number of remaining clusters was found.

5.3 Thermal Ageing of Ringhals R4 Pressurizer Weld Metal

The Ringhals R4 pressurizer was studied after operation at 345 °C for 28 years in *Paper III*, and in *Paper IV*, where it is compared to the irradiated surveillance material. It was found that thermal ageing at this temperature resulted in clusters with an average diameter of 1.9 ± 0.3 nm forming, containing Ni, Mn, Si and Cu. Cluster formation at these temperatures in low Cu materials was not expected. The clusters are located mainly at dislocations, that were present from fabrication, see Figure 5.3. The number density is smaller than for the irradiated materials, $0.16 \pm 0.05 \cdot 10^{23}$ clusters/m^3. Furthermore, the cluster distribution is heterogeneous, as the dislocations are not evenly distributed within the weld metal. The first 300 nm in Figure 5.3 contain no Mo-enriched dislocations, and the number of clusters in this volume is much lower than in the volume with dislocations. The hardness of the material increased with $\Delta\text{HV} = 32 \pm 7\,\text{kg/mm}^2$, an increase that is attributed to the clusters, as P segregation to grain boundaries also occuring during thermal ageing should give a non-hardening contribution to the embrittlement [17, 18]. When the pressurizer weld was annealed at 620 °C for one hour (simulating PWHT), the initial hardness was regained, presumably mainly due to cluster dissolution.

In addition to clusters on dislocations, there were also clusters containing Ni, Mn, Si and Cu nucleated on other clusters, presumably carbonitrides, containing V, and sometimes Cr. These carbonitrides were found in irradiated and thermally aged material, both before and after ageing, see Figure 5.4. The number of V, Cr, N, and C atoms in these clusters varies, as seen in the figure. The number density of these features is low; in many analyses no carbonitrides at all were found. They are not believed to be affected by the ageing in any

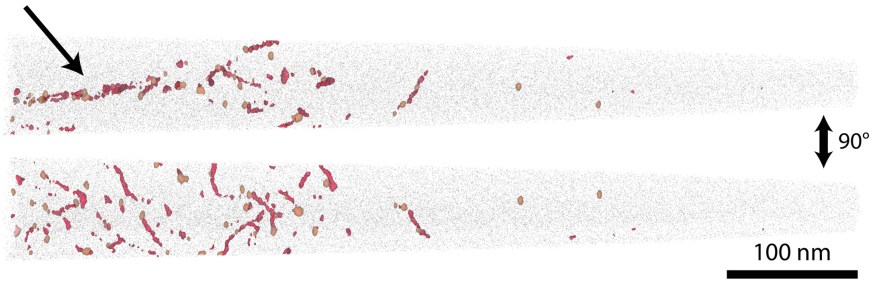

Figure 5.3: Reconstruction of APT analysis of the pressurizer. Orange surfaces correspond to 1.1 at.% Cu, and red surfaces to 2.0 at.% Mo. The arrow indicates a plane of dislocations decorated with clusters. Figure from *Paper III* [148].

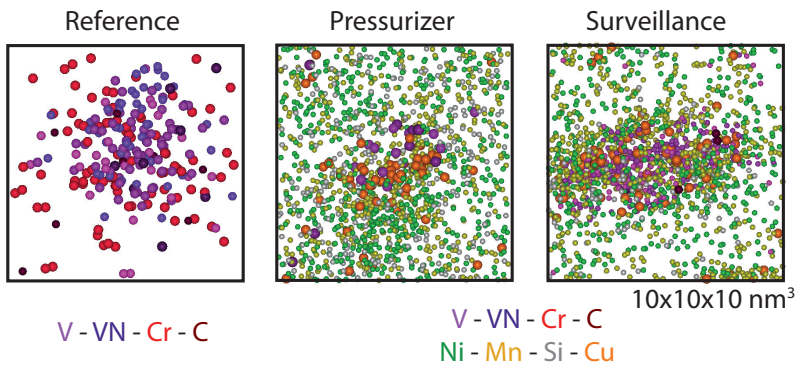

Figure 5.4: Examples of the V-containing clusters, in reference material, thermally aged pressurizer, and the surveillance material. In the reference material, only V, VN, Cr and C are shown in a cube with 10 nm sides. In the aged materials, Ni, Mn, Si and Cu are also included.

other way than acting as points of nucleation for the NiMnSi-rich clusters.

The cluster composition profile of the pressurizer is shown in Figure 5.5. The composition is compared with the surveillance material cluster profile. There is a very clear Cu-rich core of the pressurizer clusters, surrounded by Ni and Mn. The Si content in the thermally aged clusters is low in comparison to the irradiated material. There is also a difference in the Ni/Mn ratio, which is around one for the clusters in the pressurizer, but 2.4 for the surveillance material (corresponding ratios for material H6.4 is 1.7 and for H2.0 1.4). One possible explanation might be the differences in thermal diffusion and irradiation enhanced diffusion for the different atoms. Thermal diffusion is driven by vacancies only, but during irradiation, there are also interstitials that are affecting the diffusion, in case of P and Mn transport by the dumbbell mechanism [56]. PIA for 24 h at 405 °C and higher temperatures also change the

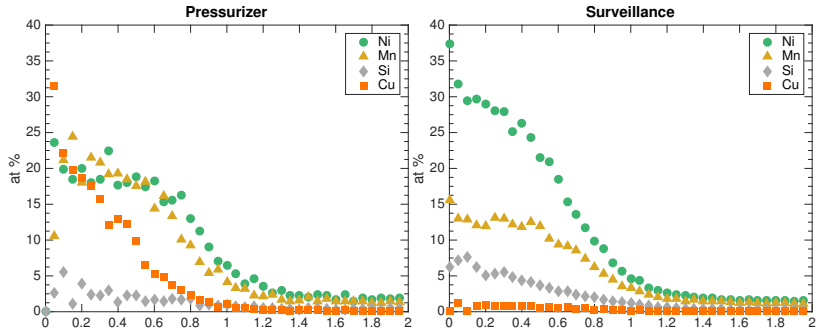

Figure 5.5: Normalised cluster composition profiles for the pressurizer and the surveillance material welds. The x-axis represents the relative radius, i. e. 1 corresponds to the cluster edge, and 0 to the cluster centre. Figure from *Paper IV* [149].

cluster Ni/Mn ratio to around one. The total amount of Ni, Mn and Si in the materials are similar, making this an effect of the ageing conditions rather than initial chemistry.

The results of the pressurizer show that there will be effects of annealing of the irradiated materials also at lower temperatures than 405 °C, given long enough times. At 345 °C, clusters nucleate on dislocations and grow slowly (after 28 years there are clusters, for other times the evolution is currently unknown), at 405 °C, most of the Ni, Mn and Si leaves the clusters within 24 h, and Cu-rich clusters coarsen. At 420 °C the clusters dissolve. In other words, the impact of thermal ageing and annealing over time is complex.

A central question is the difference between the thermally aged and the irradiated RPV welds regarding the nucleation of the clusters. In the thermally aged materials, it appears that the clusters nucleate on a range of different features; boundaries, dislocations and small vanadium carbonitrides, and a few clusters directly in the matrix. In the irradiated materials, defects are provided to nucleate on in the matrix, as the neutron irradiation result in matrix defects, such as small clusters of vacancies and interstitial loops. Vacancies has previously been observed by positron annihilation spectroscopy (PAS) to be associated with Cu in Fe-Cu model alloys, acting as points of nucleation [150]. Interstitial loops have been found to be the nucleation points of clusters and results match cluster number densities in Ringhals surveillance materials in the object kinetic Monte Carlo model by Messina et al. and Chiapetto et al. [59, 151]. In thermally aged RPV welds with higher Cu content, clusters have been found to be homogeneously distributed within the matrix [84, 88], thus indicating the Cu content as important for nucleation. In the low Cu Ringhals R4 pressurizer welds, any dislocation or other feature is attractive

for nucleation of clusters.

5.4 Degradation Phenomena in Austenitic Welds

The degradation in the ferrite of the austenitic welds in the HL material from Ringhals R2 and the irradiated Zorita core barrel (*Paper VI*) is of a different nature than in the RPV, due to the much higher Cr content. The ferrite spinodally decomposes into Fe-rich and Cr-rich volumes. Already after irradiation to 0.15 dpa (material CB-0.15) the effect is almost saturated, and no difference can be seen between irradiation to 1 (CB-1) and 2 dpa (CB-2) in the ferrite. The G-phase formation differs from material CB-0.15 to CB-1 and CB-2, where the clusters are more well-defined.

In the austenite of the irradiated materials, small P clusters are found after irradiation to 0.15 dpa. In the CB-1 and CB-2 materials, Ni-Si precipitates were found, as well as loops enriched in Ni and Si. The Ni/Si ratios of the precipitates and loop segregations were found to be between 1.6 and 2.7. In the thermally aged materials, the austenite was found to be unaffected by ageing.

The ferrite/austenite boundaries were affected by ageing. The amount of Ni and Si segregating to the interface increased with dose. In CB-1 and CB-2, the Ni and Si form elongated precipitates on the boundary, similar to those found at a low angle grain boundary. The distribution of other solute elements such as P is also found to vary dependent on dose. The P content on the interface is higher in CB-0.15 than in CL. However, CB-1 and CB-2 show a decreasing trend in boundary P content.

In the CL material, thermally aged at a temperature similar to the temperature of the irradiated materials, no spinodal decomposition or G-phase precipitation is detected. The distribution of elements in the austenite is found to be random after thermal ageing. It is thus concluded that the irradiation plays a crucial role in the degradation of the welds. The work on the austenitic welds is ongoing, and the results will be further complemented by more characterisation techniques in order to be able to discuss the degradation and the impact on properties in detail.

5.5 Conclusions

This thesis contributes to understanding the behaviour of high Ni and Mn, low Cu, RPV weld metals under neutron irradiation, and the difference in cluster characteristics when irradiated at high fluxes. The increase in cluster number density and size is gradual in the Ringhals R4 welds, and does not appear to

accelerate at high fluences. Thus, the results do not implicate the presence of so called *late blooming phases* in the material, but rather a continuous (but retarding) precipitation and growth for the fluences analysed. The use of a higher flux (lead factors up to 75) to simulate the neutron irradiation in a PWR in operation results in similar hardening as in the surveillance material, due to slightly smaller clusters with a slightly higher number density forming. A small part of the contribution to hardness probably comes from matrix defects that are behaving differently dependent on flux.

Furthermore, long term thermal ageing of the Ringhals R4 pressurizer welds, which have similar composition as the RPV welds, results in clusters located mainly on dislocations. The number density of these is one order of magnitude lower than in the irradiated welds, but the clusters' size is similar, and the compositions of the clusters are similar but irradiated clusters contain less Cu, as expected from other studies. All these results are relevant in the context of comparing microstructural observations with both atomistic studies and the large scale mechanical properties of the materials, in order to further understand the mechanisms of degradation and the effects on properties.

The austenitic welds with remaining ferrite show the multiple types of degradation occurring in components exposed to both irradiation and heat in a reactor in operation. After irradiation to 0.15 dpa, the microstructure of the ferrite of the weld was strongly affected by irradiation. Due to the complexity when many phenomena are occurring, this part of the project needs further work to be concluded.

CHAPTER 6

Outlook

Based on the conclusions in the previous chapter and the knowledge within the field, the following complementary investigations are suggested.

- In order to further study the effect of flux, an actual RPV that has been in operation could be studied. No reactor with the high Ni and Mn, and low Cu content has been analysed after decommissioning using APT so far.
- A further investigation of the matrix damage, and its contribution to mechanical properties in the high Ni and Mn RPV materials. In the Halden irradiated RPV welds, part of the hardness increase during irradiation is probably from matrix damage. However, the methodology of using hardness measurements and APT is indirect, and direct measurements such as PAS and possibly also simulations would be of value. Furthermore, in this project nothing could be concluded using only APT and hardness measurements on the matrix damage in the surveillance material, thus further understanding would be useful.
- Understanding the differences in the compositions of the irradiated clusters, and how these differences compare to the composition of the clusters in the thermally aged pressurizer would be interesting. It would be in-

teresting to compare the APT results with for instance modelling results to understand more of the mechanisms behind the differences.

- The austenitic welds need to be further characterised using TEM in order to obtain larger field of view to make more general conclusions of the degradation.

CHAPTER 7

Acknowledgements

The Swedish Centre for Nuclear Technology (SKC) is acknowledged for funding. Vattenfall Ringhals is acknowledged for providing the irradiated materials and VTT for cutting the hot materials and sending them to us. The Nordic Nuclear Safety Research (NKS) collaboration is acknowledged for funding. Furthermore, the Electric Power Research Institute (EPRI) is acknowledged for funding and for the irradiated material for the Zorita project. The Swedish Radiation Safety Authority (SSM) is also acknowledged for funding.

On a personal level, I would like to thank my supervisor Mattias Thuvander. You have been helpful with many things, from practical advice in the lab and in terms of discussions on interpretations, analysis, results, possible ways forward and ideas. Thank you for your time and curiosity, and taking my side! Also, thank you Krystyna Stiller for being my co-supervisor, and sharing your energy and enthusiasm!

I am very thankful to Pål Efsing (Vattenfall and KTH) and Jenny Roudén, Ringhals. Magnus Boåsen at Solid Mechanics, KTH, thank you for the collaboration, helping me with the connection between my results and the "real", large-scale world, and the many discussions on the RPV material. Also thank you for the good company during trips and meetings!

Furthermore, thank you Martin Bjurman (KTH and Studsvik) for the collaboration on the Zorita materials.

Thank you Ulla Ehrnstén, VTT, and Grace Burke, University of Manchester, for fruitful discussions and support!

Here at Chalmers, I would like to thank Stefan Allard and Anders Nordlund for helping me with transports of my materials, and storage. Furthermore, thank you Burcak Ebin for help with the annealing.

Dear collegues; former and present colleagues in the M2 and EOG divisions and CMAL; what would the coffee breaks be without you? You make working here very enjoyable! I would like to specially thank Anders, Stefan, Katarina and Reza for help in the lab, and Ola for invaluable help with my computer in times of crisis. Thank you Lena for the introduction to the world of electron microscopy! My former long-time office mate Masoud: thank you for your generosity and the good times, and letting me have the desk by the window!

I would also like to thank my family; my parents Karin and Erik and my sister Anna-Märta, and Karl. Last but not least, thank you Mikael for being who you are, and supporting me when I have a hard time.

Kristina Lindgren

Göteborg, November 2018

Bibliography

[1] Interngovermental Panel on Climate Change (IPCC). Global warming of 1.5 °C - an IPCC special report on the impacts of global warming of 1.5 °C above pre-industrial levels and related global greenhouse gas emission pathways, in the context of strengthening the global response to the threat of climate change, sustainable development, and efforts to eradicate poverty. Report, 2018.

[2] Key world energy statistics. Report, International Energy Agency, 2016.

[3] Statistiska Centralbyrån (SCB). *80 procent av elen kommer från vattenkraft och kärnkraft - http://www.scb.se/hitta-statistik/sverige-i-siffror/miljo/energi/, accessed 02-11-2018*. 2018.

[4] SSM. Investigation of long-term safety in the Swedish nuclear power industry and measures owing to the accident at Fukushima Dai-ichi. Report, Strålsäkerhetsmyndigheten (Swedish Radiation Safety Authority), 2013.

[5] P. Efsing and P. Ekström. *Swedish RPV Surveillance Programs*, book section Stp160320170012, pages 219–231. ASTM International, West Conshohocken, 2018.

[6] P. Efsing, C. Jansson, T. Mager, and G Embring. Analysis of the ductile-to-brittle transition temperature shift in a commercial power plant with high nickel containing weld material. *Journal of ASTM International*, 4(7), 2007.

[7] G. R. Odette and G. E. Lucas. Recent progress in understanding reactor pressure vessel steel embrittlement. *Radiation Effects and Defects in Solids*, 144(1-4):189–231, 1998.

[8] P. Efsing, J. Roudén, and P. Nilsson. Flux effects on radiation induced aging behaviour of low alloy steel weld material with high nickel and manganese content. *Effects of radiation on nuclear materials*, 26:119–134, 2014.

[9] Wolfgang Hoffelner. *Materials for Nuclear Plants: From Safe Design to Residual Life Assessments*. Springer, London, 2013.

[10] M. Hernández-Mayoral and M. J. Caturla. *Microstructure evolution of irradiated structural materials in nuclear power plants*, book section 8, pages 189–235. Woodhead Publishing Series in Energy. Woodhead Publishing, Cambridge, 2010.

[11] *Irradiation Embrittlement of Reactor Pressure Vessels (RPVs) in Nuclear Power Plants*. Woodhead Publishing, 2015.

[12] H.K.D.H. Bhadeshia and R.W.K. Honeycombe. *Steels Microstructure and properties*. Butterworth-Heinemann, 3 edition, 2006.

[13] G. R. Odette and G. E. Lucas. Embrittlement of nuclear pressure vessels. *Journal of Microscopy*, 53(7):18–22, 2001.

[14] M. K. Miller, P. Pareige, and M. G. Burke. Understanding pressure vessel steels: An atom probe perspective. *Materials Characterization*, 44(1-2):235–254, 2000.

[15] Vattenfall. *Tekniska Data Ringhals, https://corporate.vattenfall.se/globalassets/sverige/om-vattenfall/om-oss/var-verksamhet/ringhals/pdf-ovriga/tekniska-data-utforlig-info-151207.pdf, accessed 14-10-2016*. 2016.

[16] Vattenfall. *Vad visar tryckhållaren? https://corporate.vattenfall.se/press-och-media/nyheter/import-nyheter/vad-visar-tryckhallaren/, accessed 16-08-2018*. Vattenfall, 2012.

[17] H. Nakata, K. Fujii, K. Fukuya, R. Kasada, and A. Kimura. Grain boundary phosphorus segregation in thermally aged low alloy steels. *Journal of Nuclear Science and Technology*, 43(7):785–793, 2006.

[18] Y. I. Shtrombakh, B. A. Gurovich, E. A. Kuleshova, D. A. Maltsev, S. V. Fedotova, and A. A. Chernobaeva. Thermal ageing mechanisms of VVER-1000 reactor pressure vessel steels. *Journal of Nuclear Materials*, 452(1-3):348–358, 2014.

[19] B. A. Gurovich, A. A. Chernobaeva, D. Yu Erak, E. A. Kuleshova, D. A. Zhurko, V. B. Papina, M. A. Skundin, and D. A. Maltsev. Chemical composition effect on VVER-1000 RPV weld metal thermal aging. *Journal of Nuclear Materials*, 465:540–549, 2015.

[20] M. Brumovsky. *Irradiation hardening and materials embrittlement in light water reactor (LWR) environments*, book section 11, pages 357–373. Woodhead Publishing Series in Energy. Woodhead Publishing, Cambridge, 2010.

[21] T. Toyama, Y. Nagai, Z. Tang, M. Hasegawa, A. Almazouzi, E. van Walle, and R. Gerard. Nanostructural evolution in surveillance test specimens of a commercial nuclear reactor pressure vessel studied by three-dimensional atom probe and positron annihilation. *Acta Materialia*, 55(20):6852–6860, 2007.

[22] J. C. van Duysen, J. Bourgoin, P. Moser, and C. Janot. Study by positron annihilation of neutron damage in a pressurized water reactor (PWR)pressure vessel steel after a 13-year irradiation in the CHOOZ A reactor surveillance program. *ASTM STP 1170*, pages 132–138, 1993.

[23] J. C. van Duysen and G. Meric de Bellefon. 60th anniversary of electricity production from light water reactors: Historical review of the contribution of materials science to the safety of the pressure vessel. *Journal of Nuclear Materials*, 484:209–227, 2017.

[24] R. Chaouadi and R. Gérard. Copper precipitate hardening of irradiated rpv materials and implications on the superposition law and re-irradiation kinetics. *Journal of Nuclear Materials*, 345(1):65–74, 2005.

[25] M. Shimodaira, T. Toyama, K. Yoshida, K. Inoue, N. Ebisawa, K. Tomura, T. Yoshiie, M. J. Konstantinovic, R. Gérard, and Y. Nagai. Contribution of irradiation-induced defects to hardening of a low-copper reactor pressure vessel steel. *Acta Materialia*, 155:402–409, 2018.

[26] G. S. Was. *Fundamentals of Radiation Materials Science*. Springer, Berlin, 2007.

[27] G. R. Odette, T. Yamamoto, and D. Klingensmith. On the effect of dose rate on irradiation hardening of RPV steels. *Philosophical Magazine*, 85(4-7):779–797, 2005.

[28] A. Kryukov, L. Debarberis, A. Ballesteros, V. Krsjak, R. Burcl, S. V. Rogozhkin, A. A. Nikitin, A. A. Aleev, A. G. Zaluzhnyi, V. I. Grafutin, O. Ilyukhina, Yu V. Funtikov, and A. Zeman. Integrated analysis of WWER-440 RPV weld re-embrittlement after annealing. *Journal of Nuclear Materials*, 429(1-3):190–200, 2012.

[29] M. G. Burke, R. J. Stofanak, J. M. Hyde, C. A. English, and W. L. Server. Microstructural aspects of irradiation damage in A508 Gr 4N forging steel: Composition and flux effects. *Journal of ASTM International*, 1(4):1–14, 2004.

[30] R. Chaouadi and R. Gérard. Neutron flux and annealing effects on irradiation hardening of RPV materials. *Journal of Nuclear Materials*, 418(1-3):137–142, 2011.

[31] R. Chaouadi and R. Gérard. Confirmatory investigations on the flux effect and associated unstable matrix damage in RPV materials exposed to high neutron fluence. *Journal of Nuclear Materials*, 437(1-3):267–274, 2013.

[32] G. R. Odette and R. K Nanstad. Predictive reactor pressure vessel steel irradiation embrittlement models: issues and opportunities. *JOM*, 61(7):17–23, 2009.

[33] G. R. Odette and B. D. Wirth. A computational microscopy study of nanostructural evolution in irradiated pressure vessel steels. *Journal of Nuclear Materials*, 251:157–171, 1997.

[34] G. R. Odette. Radiation induced microstructural evolution in reactor pressure vessel steels. *Materials Research Society Symposium Proceedings*, 373:137–148, 1995.

[35] J. M. Hyde and C. A. English. An analysis of the structure of irradiation induced Cu-enriched clusters in low and high nickel welds. In *Materials Research Society Symposium*, volume 650, pages R6.6.1–R6.6.12, 2000.

[36] A. Wagner, A. Ulbricht, F. Bergner, and E. Altstadt. Influence of the copper impurity level on the irradiation response of reactor pressure vessel steels investigated by SANS. *Nuclear Instruments and Methods in Physics Research Section B: Beam Interactions with Materials and Atoms*, 280:98–102, 2012.

[37] P. Pareige, J. C. van Duysen, and P. Auger. An APFIM study of the microstructure of a ferrite alloy after high fluence neutron irradiation. *Applied Surface Science*, 67(1-4):342–347, 1993.

[38] P. Auger, P. Pareige, S. Welzel, and J-C Van Duysen. Synthesis of atom probe experiments on irradiation-induced solute segregation in french ferritic pressure vessel steels. *Journal of Nuclear Materials*, 280(3):331–344, 2000.

[39] M. K. Miller and K. F. Russell. Embrittlement of RPV steels: An atom probe tomography perspective. *Journal of Nuclear Materials*, 371(1-3):145–160, 2007.

[40] M. K. Miller, R. K. Nanstad, M. A. Sokolov, and K. F. Russell. The effects of irradiation, annealing and reirradiation on RPV steels. *Journal of Nuclear Materials*, 351(1-3):216–222, 2006.

[41] P. Pareige, B. Radiguet, A. Suvorov, M. Kozodaev, E. Krasikov, O. Zabusov, and J. P. Massoud. Three-dimensional atom probe study of irradiated, annealed and re-irradiated VVER 440 weld metals. *Surface and Interface Analysis*, 36(56):581–584, 2004.

[42] U. Potapovs and J. R. Hawthorne. The effect of residual elements on the response of selected pressure-vessel steels and weldments to irradiation at 550F. *Nuclear Applications*, 6(1):27–46, 1969.

[43] Smidt F. A. and H. E. Watson. Effect of resdial elements on radiation strengthening in iron alloys, pressure vessel steels, and welds. *Metallurgical Transactions*, 3(8):2065–2073, 1972.

[44] G. R. Odette. On the mechanism of irradiation embrittlement of reactor pressure vessel steels. *Scripta Metallurgica*, 17(10):1183–1188, 1983.

[45] J. E. Zelenty. Understanding thermally induced embrittlement in low copper RPV steels utilising atom probe tomography. *Materials Science and Technology*, 31(8):981–988, 2015.

[46] P. J. Othen, M. L. Jenkins, G. D. W. Smith, and W. J. Phythian. Transmission electron microscope investigations of the structure of copper precipitates in thermally-aged Fe-Cu and Fe-Cu-Ni. *Philosophical Magazine Letters*, 64(6):383–391, 1991.

[47] E. Meslin, B. Radiguet, P. Pareige, and A. Barbu. Kinetic of solute clustering in neutron irradiated ferritic model alloys and a French pressure vessel steel investigated by atom probe tomography. *Journal of Nuclear Materials*, 399(2-3):137–145, 2010.

[48] CL. Liu, G-R. Odette, B.D. Wirth, and G.E. Lucas. A lattice Monte Carlo simulation of nanophase compositions and structures in irradiated pressure vessel Fe-Cu-Ni-Mn-Si steels. *Materials Science and Engineering*, A238:202–209, 1997.

[49] S. C. Glade, B. D. Wirth, G. R. Odette, P. Asoka-Kumar, P. A. Sterne, and R. H. Howell. Positron annihilation spectroscopy and small-angle neutron scattering characterization of the effect of Mn on the nanostructural features formed in irradiated Fe-Cu-Mn alloys. *Philosophical Magazine*, 85(4-7):629–639, 2005.

[50] R. Ngayam-Happy, C. S. Becquart, C. Domain, and L. Malerba. Formation and evolution of MnNi clusters in neutron irradiated dilute Fe alloys modelled by a first principle-based AKMC method. *Journal of Nuclear Materials*, 426(1–3):198–207, 2012.

[51] P. B. Wells, T. Yamamoto, B. Miller, T. Milot, J. Cole, Y. Wu, and G. R. Odette. Evolution of manganese–nickel–silicon-dominated phases in highly irradiated reactor pressure vessel steels. *Acta Materialia*, 80:205–219, 2014.

[52] M. K. Miller, K. A. Powers, R. K. Nanstad, and P. Efsing. Atom probe tomography characterizations of high nickel, low copper surveillance RPV welds irradiated to high fluences. *Journal of Nuclear Materials*, 437(1-3):107–115, 2013.

[53] M. K. Miller, A. A. Chernobaeva, Y. I. Shtrombakh, K. F. Russell, R. K. Nanstad, D. Y. Erak, and O. O. Zabusov. Evolution of the nanostructure of VVER-1000 RPV materials under neutron irradiation and post irradiation annealing. *Journal of Nuclear Materials*, 385(3):615–622, 2009.

[54] G. Bonny, D. Terentyev, A. Bakaev, E. E. Zhurkin, M. Hou, D. Van Neck, and L. Malerba. On the thermal stability of late blooming phases in reactor pressure vessel steels: An atomistic study. *Journal of Nuclear Materials*, 442(1–3):282–291, 2013.

[55] E. Meslin, B. Radiguet, P. Pareige, C. Toffolon, and A. Barbu. Irradiation-induced solute clustering in a low nickel FeMnNi ferritic alloy. *Experimental Mechanics*, 51(9):1453–1458, 2011.

[56] L. Messina. *Multiscale Modeling of Atomic Transport Phenomena in Ferritic Steels*. Thesis, 2015.

[57] G. Bonny, D. Terentyev, E. E. Zhurkin, and L. Malerba. Monte carlo study of decorated dislocation loops in FeNiMnCu model alloys. *Journal of Nuclear Materials*, 452(1-3):486–492, 2014.

[58] K. Yabuuchi, M. Saito, R. Kasada, and A. Kimura. Neutron irradiation hardening and microstructure changes in Fe–Mn binary alloys. *Journal of Nuclear Materials*, 414(3):498–502, 2011.

[59] L. Messina, M. Chiapetto, P. Olsson, C. S. Becquart, and L. Malerba. An object kinetic Monte Carlo model for the microstructure evolution of neutron-irradiated reactor pressure vessel steels. *physica status solidi (a)*, 2016.

[60] W. Xiong, H. Ke, R. Krishnamurthy, P. Wells, L. Barnard, G. R. Odette, and D. Morgan. Thermodynamic models of low-temperature Mn–Ni–Si precipitation in reactor pressure vessel steels. *MRS Communications*, pages 1–5, 2014.

[61] D. J. Sprouster, J. Sinsheimer, E. Dooryhee, S. K. Ghose, P. Wells, T. Stan, N. Almirall, G. R. Odette, and L. E. Ecker. Structural characterization of nanoscale intermetallic precipitates in highly neutron ir-

radiated reactor pressure vessel steels. *Scripta Materialia*, 113:18–22, 2016.

[62] P. B. Wells. *The Charachter, Stability and Consequences of Mn-Ni-Si precipitates in Irraiduated Reactor Pressure Vessel Steels.* Thesis, 2016.

[63] D. J. M. King, P. A. Burr, S. C. Middleburgh, T. M. Whiting, M. G. Burke, and M. R. Wenman. The formation and structure of Fe-Mn-Ni-Si solute clusters and G-phase precipitates in steels. *Journal of Nuclear Materials*, 505:1–6, 2018.

[64] E. A. Marquis and J. M. Hyde. Applications of atom-probe tomography to the characterisation of solute behaviours. *Materials Science and Engineering: R: Reports*, 69(4-5):37–62, 2010.

[65] S. J. Zinkle and G. S. Was. Materials challenges in nuclear energy. *Acta Materialia*, 61(3):735–758, 2013.

[66] F. Bergner, A. Ulbricht, H. Hein, and M. Kammel. Flux dependence of cluster formation in neutron-irradiated weld material. *Journal of Physics: Condensed Matter*, 20(10):104262, 2008.

[67] A. Ballesteros, R. Ahlstrand, C. Bruynooghe, A. Chernobaeva, Y. Kevorkyan, D. Erak, and D. Zurko. Irradiation temperature, flux and spectrum effects. *Progress in Nuclear Energy*, 53(6):756–759, 2011.

[68] R. E. Stoller. The effect of neutron flux on radiation-induced embrittlement in reactor pressure vessel steels. *Journal of ASTM International*, 1(4):326–337, 2004.

[69] A. Wagner, F. Bergner, R. Chaouadi, H. Hein, M. Hernández-Mayoral, M. Serrano, A. Ulbricht, and E. Altstadt. Effect of neutron flux on the characteristics of irradiation-induced nanofeatures and hardening in pressure vessel steels. *Acta Materialia*, 104:131–142, 2016.

[70] K. Dohi, K. Nishida, A. Nomoto, N. Soneda, H. Matsuzawa, and M. Tomimatsu. Effect of neutron flux at high fluence on microstructural and hardness changes of RPV steels. *ASME 2010 Pressure Vessels and Piping Division K-PVP Conference*, 2010.

[71] N. Soneda, K. Nishida, A. Nomoto, and K. Dohi. Flux effect on embrittlement of reactor pressure vessel steels irradiated to high fluences. *Fontevraud 8: Conference on Contribution of Materials Investigations and Operating Experience to LWRs' Safetyy, Performance and Reliability*, 2014.

[72] K. Fukuya, K. Ohno, H. Nakata, S. Dumbill, and J. M. Hyde. Microstructural evolution in medium copper low alloy steels irradiated in a pressurized water reactor and a material test reactor. *Journal of Nuclear Materials*, 312(2-3):163–173, 2003.

[73] M.K. Miller and K.F. Russell. APFIM characterization of a high phosphorus Russian RPV weld. *Applied Surface Science*, 94/95:378–383, 1996.

[74] A. V. Nikolaeva, Y. A. Nikolaev, and Y. Kevorkyan. Grain-boundary segregation of phosphorous in low-alloy steel. *Atomic Energy*, 91(1):534–542, 2001.

[75] S. Suzuki, S. Tanii, K. Abiko, and H. Kimura. Site competition between sulfur and carbon at grain boundaries and their effects on the grain boundary cohesion in iron. *Metallurgical and Materials Transactions A*, 18 A:1109–1115, 1987.

[76] G. Tauber and H. J. Grabke. Grain boundary segregation of sulfur, nitrogen and carbon in alpha-iron. *Berichte der Bunsengesellschaft für physikalische Chemie*, 82(3):298–302, 1978.

[77] A. K. Seeger. On the theory of radiation damage and radiation hardening. *Proceedings of the Second UN Conference on Peaceful Uses of Atomic Energy*, 6:250–273, 1958.

[78] F. Bergner, F. Gillemot, M. Hernández-Mayoral, M. Serrano, G. Török, A. Ulbricht, and E. Altstadt. Contributions of Cu-rich clusters, dislocation loops and nanovoids to the irradiation-induced hardening of Cu-bearing low-Ni reactor pressure vessel steels. *Journal of Nuclear Materials*, 461:37–44, 2015.

[79] K. C. Russell and L. M. Brown. A dispersion strenghtening model based on differing elastic moduli applied to the iron-copper system. *Acta Metallurgica*, 20:969–974, 1972.

[80] P. D. Styman, J. M. Hyde, D. Parfitt, K. Wilford, M. G. Burke, C. A. English, and P. Efsing. Post-irradiation annealing of Ni–Mn–Si-enriched clusters in a neutron-irradiated RPV steel weld using atom probe tomography. *Journal of Nuclear Materials*, 459:127–134, 2015.

[81] L. Liu, K. Nishida, K. Dohi, A. Nomoto, N. Soneda, K. Murakami, Z. Li, D. Chen, and N. Sekimura. Effects of solute elements on hardening and microstructural evolution in neutron-irradiated and thermally-aged reactor pressure vessel model alloys. *Journal of Nuclear Science and Technology*, pages 1–8, 2016.

[82] N. Soneda, K. Dohi, A. Nomoto, K. Nishida, and S. Ishino. Embrittlement correlation method for the Japanese reactor pressure vessel materials. *Journal of ASTM International*, 7(3):1–20, 2010.

[83] M. Kolluri, A. Kryukov, A. J. Magielsen, P. Hähner, V. Petrosyan, G. Sevikyan, and Z. Szaraz. Mechanical properties and microstructure of long

term thermal aged WWER 440 RPV steel. *Journal of Nuclear Materials*, 486:138–147, 2017.

[84] P. D. Styman, J. M. Hyde, A. Morley, K. Wilford, N. Riddle, and G. D. W. Smith. The effect of Ni on the microstructural evolution of high Cu reactor pressure vessel steel welds after thermal ageing for up to 100,000 h. *Materials Science and Engineering: A*, 736:111–119, 2018.

[85] P. D. Styman, J. M. Hyde, K. Wilford, A. Morley, and G. D. W. Smith. Precipitation in long term thermally aged high copper, high nickel model RPV steel welds. *Progress in Nuclear Energy*, 57:86–92, 2012.

[86] A. Seko, N. Odagaki, S. R. Nishitani, I. Tanaka, and H. Adachi. Free-energy calculation of precipitate nucleation in an Fe-Cu-Ni alloy. *Materials Transactions*, 45(7):1978–1981, 2004.

[87] A. T. Al-Motasem, M. Posselt, and F. Bergner. Nanoclusters in bcc-Fe containing vacancies, copper and nickel: Structure and energetics. *Journal of Nuclear Materials*, 418(1-3):215–222, 2011.

[88] J. M. Hyde, G. Sha, E. A. Marquis, A. Morley, K. B. Wilford, and T. J. Williams. A comparison of the structure of solute clusters formed during thermal ageing and irradiation. *Ultramicroscopy*, 111(6):664–71, 2011.

[89] Q. Liu, J. Gu, and W. Liu. On the role of Ni in Cu precipitation in multicomponent steels. *Metallurgical and Materials Transactions A*, 44(10):4434–4439, 2013.

[90] J. T. Buswell, C. A. English, M. G. Hetherington, W. J. Phythian, G. D. W. Smith, and G. M. Worrall. An analysis of small clusters formed in thermally aged and irradiated FeCu and FeCuNi model alloys. *Effects of radiation on nuclear materials: 14th international symposium*, 2:127–153, 1990.

[91] A. Etienne, B. Radiguet, P. Pareige, J. P. Massoud, and C. Pokor. Tomographic atom probe characterization of the microstructure of a cold worked 316 austenitic stainless steel after neutron irradiation. *Journal of Nuclear Materials*, 382(1):64–69, 2008.

[92] Z. Jiao and G. S. Was. Novel features of radiation-induced segregation and radiation-induced precipitation in austenitic stainless steels. *Acta Materialia*, 59(3):1220–1238, 2011.

[93] E. A. Kenik and J. T. Busby. Radiation-induced degradation of stainless steel light water reactor internals. *Materials Science and Engineering: R: Reports*, 73(7-8):67–83, 2012.

[94] Y. Chen, P. H. Chou, and E. A. Marquis. Quantitative atom probe tomography characterization of microstructures in a proton irradiated 304 stainless steel. *Journal of Nuclear Materials*, 451(1-3):130–136, 2014.

[95] D. A. Porter and K. E. Easterling. *Phase Transformations in Metals and Alloys*. Nelson Thornes, Cheltenham, second edition, 2001.

[96] J. W. Cahn. On spinodal decomposition. *Acta Metallurgica*, 9:795–801, 1961.

[97] F. Danoix and P. Auger. Atom probe studies of the Fe-Cr system and stainless steels aged at intermediate temperature: a review. *Materials Characterization*, 44:177–201, 2000.

[98] A. Pineau and J. Besson. *Thermal Embrittlement of Cast Duplex Stainless Steels: Observations and Modelling*, book section 5, pages 161–208. 2013.

[99] W. Xiong, P. Hedström, M. Selleby, J. Odqvist, M. Thuvander, and Q. Chen. An improved thermodynamic modeling of the Fe–Cr system down to zero kelvin coupled with key experiments. *Calphad*, 35(3):355–366, 2011.

[100] P. Hedström, F. Huyan, J. Zhou, S. Wessman, M. Thuvander, and J. Odqvist. The $475^{\circ}c$ embrittlement in Fe–20Cr and Fe–20Cr–X (X=Ni, Cu, Mn) alloys studied by mechanical testing and atom probe tomography. *Materials Science and Engineering: A*, 574:123–129, 2013.

[101] M. K. Miller, R. E. Stoller, and K. F. Russell. Effect of neutron-irradiation on the spinodal decomposition of Fe-32% Cr model alloy. *Journal of Nuclear Materials*, 230:219–225, 1996.

[102] F. Soisson and T. Jourdan. Radiation-accelerated precipitation in Fe–Cr alloys. *Acta Materialia*, 103:870–881, 2016.

[103] J. Bentley, M.K. Miller, S.S. Brenner, and J.A. Spitznagel. Identification of G-phase in aged cast CF 8 type stainless steel. *Proceedings - Annual Meeting, Electron Microscopy Society of America*, 43:328–329, 1985.

[104] F. Danoix, P. Auger, and D. Blavette. An atom-probe investigation of some correlated phase transformations in Cr, Ni, Mo containing supersaturated ferrites. *Surface Science*, 266(1-3):364–369, 1992.

[105] A. Mateo, L. Llanes, M. Anglada, A. Redjaimia, and G. Metauer. Characterization of the intermetallic G-phase in an AISI 329 duplex stainless steel. *Journal of Materials Science*, 32(17):4533–4540, 1997.

[106] C. Pareige, J. Emo, S. Saillet, C. Domain, and P. Pareige. Kinetics of G-phase precipitation and spinodal decomposition in very long aged ferrite of a Mo-free duplex stainless steel. *Journal of Nuclear Materials*, 465:383–389, 2015.

[107] F. Danoix, P. Bas, J. P. Massoud, Guttermanm M., and P. Auger. Atom probe and transmission electron microscopy study of reverted stainless steels. *Applied Surface Science*, 67:348–355, 1993.

[108] T. R. Leax, S.S. Brenner, and J.A. Spitznagel. Atom probe examination of thermally aged CF8M cast stainless steel. *Metallurgical Transactions A*, 23A:2725–2736, 1992.

[109] W. Guo, D. A. Garfinkel, J. D. Tucker, D. Haley, G. A. Young, and J. D. Poplawsky. An atom probe perspective on phase separation and precipitation in duplex stainless steels. *Nanotechnology*, 27(25):254004, 2016.

[110] C. Pareige, S. Novy, S. Saillet, and P. Pareige. Study of phase transformation and mechanical properties evolution of duplex stainless steels after long term thermal ageing (>20years). *Journal of Nuclear Materials*, 411(1-3):90–96, 2011.

[111] S. Mburu, R. P. Kolli, D. E. Perea, S. C. Schwarm, A. Eaton, J. Liu, S. Patel, J. Bartrand, and S. Ankem. Effect of aging temperature on phase decomposition and mechanical properties in cast duplex stainless steels. *Materials Science and Engineering: A*, 690:365–377, 2017.

[112] R. M. Boothby, J. M. Hyde, H. Swan, D. Parfitt, K. Wilford, and P. Lindner. SANS examination of irradiated RPV steel welds during in-situ annealing. *Journal of Nuclear Materials*, 461:45–50, 2015.

[113] F. Bergner, A. Ulbricht, and H. W. Viehrig. Acceleration of irradiation hardening of low-copper reactor pressure vessel steel observed by means of SANS and tensile testing. *Philosophical Magazine Letters*, 89(12):795–805, 2009.

[114] A. Ulbricht, E. Altstadt, F. Bergner, H. W. Viehrig, and U. Keiderling. Small-angle neutron scattering investigation of as-irradiated, annealed and reirradiated reactor pressure vessel weld material of decommissioned reactor. *Journal of Nuclear Materials*, 416(1-2):111–116, 2011.

[115] R. G. Carter, N. Soneda, K. Dohi, J. M. Hyde, C. A. English, and W. L. Server. Microstructural characterization of irradiation-induced Cu-enriched clusters in reactor pressure vessel steels. *Journal of Nuclear Materials*, 298:211–224, 2001.

[116] P. D. Edmondson, C. M. Parish, and R. K. Nanstad. Using complimentary microscopy methods to examine Ni-Mn-Si-precipitates in highly-irradiated reactor pressure vessel steels. *Acta Materialia*, 134:31–39, 2017.

[117] S. Lozano-Perez, G. Sha, J. M. Titchmarsh, M. L. Jenkins, S. Hirosawa, A. Cerezo, and G. D. W. Smith. Comparison of the number densities of nanosized Cu-rich precipitates in ferritic alloys measured using EELS and EDX mapping, HREM and 3DAP. *Journal of Materials Science*, 41(9):2559–2565, 2006.

[118] J. J. H. Lim, J. M. Hyde, S. Lozano-Perez, and C. R. M. Grovenor. Microstructural characterization of irradiation-induced MnNi-rich solute cluster in highly neutron-irradiated MnNiMo alloyed weld metals. *Effects of Radiation on Nuclear Materials*, 26:57–73, 2014.

[119] M. K. Miller. *Atom Probe Tomography: Analysis at the Atomic Level*. Kluwer Academic/Plenum Publishers, New York, 2000.

[120] B. Gault, M. P. Moody, J. M. Cairney, and S. P. Ringer. *Atom Probe Microscopy*. Springer, New York, 2012.

[121] M. K. Miller and R. G. Forbes. *Atom-Probe Tomography: The Local Electrode Atom Probe*. Springer, New York, 2014.

[122] P. Bas, A. Bostel, B. Deconihout, and D. Blavette. A general protocol for the reconstruction of 3D atom probe data. *Applied Surface Science*, 87/88:298–304, 1995.

[123] O. C. Hellman, J. A. Vandenbroucke, J. Rüsing, D. Isheim, and D. N. Seidman. Analysis of three-dimensional atom-probe data by the proximity histogram. *Microscopy and Microanalysis*, 6(5):437–444, 2000.

[124] A. Heinrich, T. Al-Kassab, and R. Kirchheim. Investigation of the early stages of decomposition of Cu–0.7at.% Fe with the tomographic atom probe. *Materials Science and Engineering: A*, 353(1-2):92–98, 2003.

[125] D. Vaumousse, A. Cerezo, and P.J. Warren. A procedure for quantification of precipitate microstructures from three-dimensional atom probe data. *Ultramicroscopy*, 95:215–221, 2003.

[126] J. S. Langer, M. Bar-on, and Harold D. Miller. New computational method in the theory of spinodal decomposition. *Physical Review A*, 11(4):1417–1429, 1975.

[127] J. Zhou, J. Odqvist, M. Thuvander, and P. Hedstrom. Quantitative evaluation of spinodal decomposition in Fe-Cr by atom probe tomography and radial distribution function analysis. *Microsc Microanal*, 19(3):665–75, 2013.

[128] J. M. Hyde, M. G. Burke, B. Gault, D. W. Saxey, P. Styman, K. B. Wilford, and T. J. Williams. Atom probe tomography of reactor pressure vessel steels: an analysis of data integrity. *Ultramicroscopy*, 111(6):676–82, 2011.

[129] B. Gault, F. Danoix, K. Hoummada, D. Mangelinck, and H. Leitner. Impact of directional walk on atom probe microanalysis. *Ultramicroscopy*, 113:182–191, 2012.

[130] M. K. Miller and M. G. Hetherington. Local magnification effects in the atom probe. *Surface Science*, 246(1-3):442–449, 1991.

[131] F. Vurpillot, A. Bostel, and D. Blavette. Trajectory overlaps and local magnification in three-dimensional atom probe. *Applied Physics Letters*, 76(21):3127–3129, 2000.

[132] A. Morley, G. Sha, S. Hirosawa, A. Cerezo, and G. D. Smith. Determining the composition of small features in atom probe: bcc Cu-rich precipitates in an Fe-rich matrix. *Ultramicroscopy*, 109(5):535–40, 2009.

[133] S. Shu, B. D. Wirth, P. B. Wells, D. D. Morgan, and G. R. Odette. Multi-technique characterization of the precipitates in thermally aged and neutron irradiated Fe-Cu and Fe-Cu-Mn model alloys: Atom probe tomography reconstruction implications. *Acta Materialia*, 146:237–252, 2018.

[134] S. Lozano-Perez, J. M. Titchmarsh, and M. L. Jenkins. Determination of the Fe content of embedded Cu-rich particles in ferritic alloys using energy-filtered TEM. *Ultramicroscopy*, 106(2):75–91, 2006.

[135] M. Thuvander, J. Weidow, J. Angseryd, L. K. Falk, F. Liu, M. Sonestedt, K. Stiller, and H. O. Andren. Quantitative atom probe analysis of carbides. *Ultramicroscopy*, 111(6):604–8, 2011.

[136] D. J. Larson, D. T. Foord, A. K. Petford-Long, H. Liew, M. G. Blamire, A. Cerezo, and G. D. W. Smith. Field-ion specimen preparation using focused ion-beam milling. *Ultramicroscopy*, 79(1-4):287–293, 1999.

[137] K. Thompson, D. Lawrence, D. J. Larson, J. D. Olson, T. F. Kelly, and B. Gorman. In situ site-specific specimen preparation for atom probe tomography. *Ultramicroscopy*, 107(2-3):131–9, 2007.

[138] J. Blomström, P. Efsing, J. Roudén, A. Karlsson, and P. Nilsson. Ringhals 3 and 4 – from problem to solution - managing ageing of RPV weld with high Ni and Mn-content for long term irradiation. *Proceedings - Fontevraud 9: Contribution of Materials Investigations and Operating Experience to Light Water NPPs' Safety, Performance and Reliability*, 2018.

[139] J. M. Hyde, R. M. Boothby, H. Swan, N. Riddle, K. Wilford, M. G. Burke, and P. Efsing. A sensitivity study using maximum entropy to interpret SANS data from the Ringhals Unit 3 NPP. *Journal of Nuclear Materials*, 509:417–424, 2018.

[140] M. Boåsen, P. Efsing, and U. Ehrnstén. On flux effects in a low alloy steel from a Swedish reactor pressure vessel. *Journal of Nuclear Materials*, 484:110–119, 2017.

[141] M. Boåsen, K. Lindgren, J. Roudén, M. Öberg, J. Faleskog, M. Thuvander, and P. Efsing. Thermal ageing of low alloy steel weldments from a swedish nuclear power plant – a study of mechanical properties. *Proceedings - Fontevraud 9: Contribution of Materials Investigations and Operating Experience to Light Water NPPs' Safety, Performance and Reliability*, 2018.

[142] M. Bjurman, K. Lindgren, M. Thuvander, P. Ekström, and P. Efsing. Microstructural evolution of welded stainless steels on integrated effect of thermal aging and low flux irradiation. *the 18th International Conferece on Environmental Degradation of Materials in Nucler Power Systems - Water Reactors*, pages 703–710, 2018.

[143] M. Bjurman, M. Thuvander, K. Lindgren, and P. Efsing. Thermal ageing and irradiation of cast and welded stainless steels and the influence on LTO. *Proceedings - Fontevraud 9: Contribution of Materials Investigations and Operating Experience to Light Water NPPs' Safety, Performance and Reliability*, 2018.

[144] M. Bjurman, B. Forssgren, and P. Efsing. *Fracture Mechanical Testing of In-Service Thermally Aged Cast Stainless Steel*, pages 58–80. ASTM international, West Conshohocken, PA, 2017.

[145] A. Jenssen, J. Stjärnsäter, K. Kese, R. Carter, J. Smith, A. Demma, and M. Hiser. Fracture toughness testing of an irradiated PWR core barrel weld. *Proceedings - Fontevraud 9: Contribution of Materials Investigations and Operating Experience to Light Water NPPs' Safety, Performance and Reliability*, 2018.

[146] K. Lindgren, K. Stiller, P. Efsing, and M. Thuvander. On the analysis of clustering in an irradiated low alloy reactor pressure vessel steel weld. *Microsc Microanal*, 23(2):376–384, 2017.

[147] K. Lindgren, M. Boåsen, K. Stiller, P. Efsing, and M. Thuvander. Evolution of precipitation in reactor pressure vessel steel welds under neutron irradiation. *Journal of Nuclear Materials*, 488:222–230, 2017.

[148] K. Lindgren, M. Boåsen, K. Stiller, P. Efsing, and M. Thuvander. Cluster formation in in-service thermally aged pressurizer welds. *Journal of Nuclear Materials*, 504:23–28, 2018.

[149] K. Lindgren, M. Boåsen, K. Stiller, P. Efsing, and M. Thuvander. Thermal ageing of low alloy steel weldments from a Swedish nuclear power plant – the evolution of the microstructure. *Proceedings - Fontevraud 9: Contribution of Materials Investigations and Operating Experience to Light Water NPPs' Safety, Performance and Reliability*, 2018.

[150] Y. Nagai, Z. Tang, M. Hassegawa, T. Kanai, and M. Saneyasu. Irradiation-induced Cu aggregations in Fe: An origin of embrittlement of reactor pressure vessel steels. *Physical Review B*, 63(13), 2001.

[151] M. Chiapetto, L. Messina, C. S. Becquart, P. Olsson, and L. Malerba. Nanostructure evolution of neutron-irradiated reactor pressure vessel steels: Revised object kinetic Monte Carlo model. *Nuclear Instruments and Methods in Physics Research Section B: Beam Interactions with Materials and Atoms*, 393:105–109, 2017.